CFHTLenS tomographic weak lensing: quantifying accurate redshift distributions

Jonathan Benjamin, Ludovic van Waerbeke, Catherine Heymans, Martin Kilbinger, Thomas Erben, Hendrik Hildebrandt, Henk Hoekstra, Thomas D. Kitching, Yannick Mellier, Lance Miller, et al.

Monthly Notices
of the
ROYAL ASTRONOMICAL SOCIETY

MNRAS **431,** 1547–1564 (2013) doi:10.1093/mnras/stt276
Advance Access publication 2013 March 8

CFHTLenS tomographic weak lensing: quantifying accurate redshift distributions

Jonathan Benjamin,[1]⋆ Ludovic Van Waerbeke,[1] Catherine Heymans,[2] Martin Kilbinger,[3,4,5,6] Thomas Erben,[7] Hendrik Hildebrandt,[1,7] Henk Hoekstra,[8,9] Thomas D. Kitching,[2] Yannick Mellier,[4,10] Lance Miller,[11] Barnaby Rowe,[12,13] Tim Schrabback,[7,8,14] Fergus Simpson,[2] Jean Coupon,[15] Liping Fu,[16] Joachim Harnois-Déraps,[17,18] Michael J. Hudson,[19,20] Konrad Kuijken,[8] Elisabetta Semboloni,[8] Sanaz Vafaei[1] and Malin Velander[8,11]

[1] *University of British Columbia, 6224 Agricultural Road, Vancouver, BC V6T 1Z1, Canada*
[2] *Scottish Universities Physics Alliance, Institute for Astronomy, University of Edinburgh, Royal Observatory, Blackford Hill, Edinburgh EH9 3HJ, UK*
[3] *CEA Saclay, Service d'Astrophysique (SAp), Orme des Merisiers, Bât 709, F-91191 Gif-sur-Yvette, France*
[4] *Institut d'Astrophysique de Paris, CNRS, UMR 7095, 98 bis Boulevard Arago, F-75014 Paris, France*
[5] *Excellence Cluster Universe, Boltzmannstr. 2, D-85748 Garching, Germany*
[6] *Universitäts-Sternwarte, Ludwig-Maximillians-Universität München, Scheinerstr. 1, D-81679 München, Germany*
[7] *Argelander Institute for Astronomy, University of Bonn, Auf dem Hügel 71, D-53121 Bonn, Germany*
[8] *Leiden Observatory, Leiden University, Niels Bohrweg 2, 2333 CA Leiden, the Netherlands*
[9] *Department of Physics and Astronomy, University of Victoria, Victoria, BC V8P 5C2, Canada*
[10] *Institut d'Astrophysique de Paris, Université Pierre et Marie Curie – Paris 6, 98 bis Boulevard Arago, F-75014 Paris, France*
[11] *Department of Physics, Oxford University, Keble Road, Oxford OX1 3RH, UK*
[12] *Department of Physics and Astronomy, University College London, Gower Street, London WC1E 6BT, UK*
[13] *California Institute of Technology, 1200 E California Boulevard, Pasadena, CA 91125, USA*
[14] *Kavli Institute for Particle Astrophysics and Cosmology, Stanford University, 382 Via Pueblo Mall, Stanford, CA 94305-4060, USA*
[15] *Institute of Astronomy and Astrophysics, Academia Sinica, PO Box 23-141, Taipei 10617, Taiwan*
[16] *Key Lab for Astrophysics, Shanghai Normal University, 100 Guilin Road, Shanghai 200234, China*
[17] *Canadian Institute for Theoretical Astrophysics, University of Toronto, Ontario, M5S 3H8, Canada*
[18] *Department of Physics, University of Toronto, Ontario, M5S 1A7, Canada*
[19] *Department of Physics and Astronomy, University of Waterloo, Waterloo, ON, N2L 3G1, Canada*
[20] *Perimeter Institute for Theoretical Physics, 31 Caroline Street N, Waterloo, ON, N2L 1Y5, Canada*

Accepted 2013 February 11. Received 2013 February 5; in original form 2012 December 11

ABSTRACT

The Canada–France–Hawaii Telescope Lensing Survey (CFHTLenS) comprises deep multi-colour ($u^*g'r'i'z'$) photometry spanning 154 deg^2, with accurate photometric redshifts and shape measurements. We demonstrate that the redshift probability distribution function summed over galaxies provides an accurate representation of the galaxy redshift distribution accounting for random and catastrophic errors for galaxies with best-fitting photometric redshifts $z_p < 1.3$.

We present cosmological constraints using tomographic weak gravitational lensing by large-scale structure. We use two broad redshift bins $0.5 < z_p \leq 0.85$ and $0.85 < z_p \leq 1.3$ free of intrinsic alignment contamination, and measure the shear correlation function on angular scales in the range ∼1–40 arcmin. We show that the problematic redshift scaling of the shear signal, found in previous Canada–France–Hawaii Telescope Legacy Survey data analyses, does not affect the CFHTLenS data. For a flat Λ cold dark matter model and a fixed matter density $\Omega_m = 0.27$, we find the normalization of the matter power spectrum $\sigma_8 = 0.771 \pm 0.041$. When combined with cosmic microwave background data (*Wilkinson Microwave Anisotropy*

⋆ E-mail: jonben@gmail.com

Probe 7-year results), baryon acoustic oscillation data (BOSS) and a prior on the Hubble constant from the *Hubble Space Telescope* distance ladder, we find that CFHTLenS improves the precision of the fully marginalized parameter estimates by an average factor of 1.5−2. Combining our results with the above cosmological probes, we find $\Omega_{\rm m} = 0.2762 \pm 0.0074$ and $\sigma_8 = 0.802 \pm 0.013$.

Key words: techniques: photometric – galaxies: distances and redshifts – galaxies: photometry – cosmological parameters – cosmology: observations – large-scale structure of Universe.

1 INTRODUCTION

Weak gravitational lensing by large-scale structure provides valuable cosmological information that can be obtained by analysing the apparent shapes of distant galaxies that have been coherently distorted by foreground mass (Bartelmann & Schneider 2001). Since weak lensing is sensitive to the distance–redshift relation and the time-dependent growth of structure, it is a particularly useful tool for constraining models of dark energy (Albrecht et al. 2006, 2009; Peacock et al. 2006). To measure the contribution of dark energy over time, the lensing signal must be measured at several redshifts, which is known as weak lensing tomography (see, for example, Hu 1999; Huterer 2002). Several observations of weak lensing tomography have been completed (Bacon et al. 2005; Semboloni et al. 2006; Massey et al. 2007). Most recently a study of the Cosmic Evolution Survey (COSMOS) by Schrabback et al. (2010) found evidence for the accelerated expansion of the Universe from weak lensing tomography.

Redshift information is vital to weak lensing interpretation since the distortion of light bundles is a geometric effect and the growth of structure is redshift dependent. Weak lensing data sets necessitate the use of photometric redshifts due to the large number of galaxies they contain. Spectroscopic redshifts typically exist for a small and relatively bright fraction of galaxies, providing a training set for photometric redshifts at brighter magnitudes. Several approaches for determining the redshift distribution of galaxies have been used in past weak lensing studies. Many early studies (see, for example, Van Waerbeke et al. 2002; Bacon et al. 2003; Hamana et al. 2003; Jarvis et al. 2003; Van Waerbeke, Mellier & Hoekstra 2005; Hoekstra et al. 2006; Benjamin et al. 2007; Fu et al. 2008), lacking multiband photometry, relied on external photometric redshift samples such as the *Hubble Deep Field*-North and South, and the Canada–France–Hawaii Telescope Legacy Survey (CFHTLS) Deep fields. Due to the small area of these fields, sampling variance was an important, but often neglected, source of error in these studies, as presented by Van Waerbeke et al. (2006).

Current and planned weak lensing surveys have multiband photometry enabling photometric redshift estimates for all galaxies. Methods for measuring photometric redshifts use various model-fitting techniques with the goal of finding a match between the observed photometry and template galaxy spectra which are displaced in redshift and convolved with the optical response of the filter set, telescope and camera. Depending on the set of photometric filters, degeneracies can exist between different template spectra at different redshifts. We refer to large errors in the best-fitting parameters due to mismatches under these degeneracies as catastrophic errors. The effect of catastrophic errors on weak lensing parameter constraints has been investigated in several studies, for example Ma, Hu & Huterer (2006), Bernstein & Huterer (2010) and Hearin et al. (2010). Using a detailed Fisher matrix analysis, Hearin et al. (2010) show the importance of properly characterizing catastrophic errors to dark energy parameter constraints using weak lensing tomography. The implication of neglecting these errors is not well known, although Hearin et al. (2010) argue that there are many factors governing the final impact on dark energy parameters and each survey needs to be carefully considered to make any definitive statement. It is clear that catastrophic errors will become increasingly important in the next generation of weak lensing cosmic shear surveys.

In this paper, we present a tomographic weak lensing analysis of the Canada–France–Hawaii Telescope Lensing Survey[1] (CFHTLenS), with redshifts measured in Hildebrandt et al. (2012) using the Bayesian photometric redshift code (BPZ; Benítez 2000). The BPZ analysis of the CFHTLenS photometry uses a set of six recalibrated spectral energy distribution galaxy templates from Capak et al. (2004) and a magnitude-dependent prior on the redshift distribution (see Hildebrandt et al. 2012 for further details). If the galaxy template set and prior used are an accurate and complete representation of the true galaxy population at all redshifts, then the probability distribution function (PDF) calculated using BPZ determines the true error distribution. The redshift distribution of a galaxy sample can then be calculated from the sum of the PDFs to determine an accurate redshift distribution that includes the effects of both statistical and catastrophic errors. This is in contrast to the standard method of using a histogram of photometric redshifts taken from the maximum of the posterior. We test the accuracy of the summed PDFs with overlapping spectroscopic redshifts at bright magnitudes and with resampled COSMOS-30 redshifts (Ilbert et al. 2009) at faint magnitudes. In both cases, we also assess the level of contamination between redshift bins using an angular cross-correlation technique (Benjamin et al. 2010).

Demonstrating the accuracy of the summed PDFs is of particular interest to those using the CFHTLenS data products. However, the results in this paper also contribute to a broader understanding of the use of redshift PDFs as measures of the redshift distribution. The CFHTLenS photometric redshifts are measured using BPZ (Benítez 2000); however, other methods also produce posterior PDFs such as the ZEBRA photometric redshift code (Feldmann et al. 2006) and a photometric redshift-independent method presented in Lima et al. (2008) and extended in Cunha et al. (2009). The Cunha et al. (2009) method estimates a probability distribution based on the redshifts of nearest-neighbour galaxies in multidimensional phase space. There have been several studies focused on using redshift PDFs as estimates of the redshift distribution. Brodwin et al. (2006) show that the summed PDFs of galaxies can be used instead of the maximum likelihood values, as a better estimate of the redshift distribution of galaxies. This was tested on simulated galaxy samples using a Monte Carlo technique. Using the full PDF for galaxies has been shown to dramatically reduce the weak lensing calibration bias for galaxy–galaxy lensing (Mandelbaum et al. 2008). Wittman (2009) presents a technique to estimate an unbiased redshift using the PDF of a galaxy, effectively correcting the maximum likelihood value. The work in this paper builds on these results and most notably we

[1] http://www.cfhtlens.org

will use two methods to assess the accuracy of the summed PDFs at faint magnitudes where spectroscopic redshift coverage does not exist.

Previous CFHTLS results were found to be biased, underestimating the shear at high redshifts, thus requiring the addition of a nuisance parameter when model fitting (Kilbinger et al. 2009). Furthermore, field selection was discriminated based on a cosmology-dependent criterion possibly resulting in a confirmation bias. The CFHTLenS catalogues we use in this paper have been thoroughly tested for systematic errors. These tests are cosmology insensitive and were completed without any cosmological analysis of the data (Heymans et al. 2012b). One of the primary goals of this paper is to demonstrate that the redshift scaling of the shear is consistent with expectations. We limit our cosmic shear analysis to two broad redshift bins in order to obtain parameter constraints that do not depend on the modelling of intrinsic alignment (Croft & Metzler 2000; Heavens, Refregier & Heymans 2000; Hirata & Seljak 2004). A study of cosmological constraints from CFHTLenS with several redshift bins, accounting for intrinsic alignment, is presented in Heymans et al. (2012a). Kilbinger et al. (2013) present a thorough investigation of 2D cosmic shear, including a comparison of all popular second-order shear statistics. Simpson et al. (2013) use the tomographic shear signal presented in this paper to constrain deviations from General Relativity on cosmological scales.

CFHTLenS has an effective area of 154 deg^2 with deep photometry in five broad bands $u^*g'r'i'z'$ and a 5σ point source limiting magnitude in the i' band of $i'_{\rm AB} \sim 25.5$. These data were obtained as part of the CFHTLS, which completed observations in early 2009. Heymans et al. (2012b) present an overview of the CFHTLenS analysis pipeline summarizing the weak lensing data processing with THELI (Erben et al. 2012), shear measurement with *lens*fit (Miller et al. 2013) and photometric redshift measurement from point spread function matched photometry (Hildebrandt et al. 2012) using BPZ. Each galaxy in the CFHTLenS catalogue has a shear measurement $\epsilon_{\rm obs}$, an inverse variance weight w, a PDF giving the posterior probability as a function of redshift and a photometric redshift estimate from the peak of the PDF $z_{\rm p}$. The shear calibration corrections described in Miller et al. (2013) and Heymans et al. (2012b) are applied and we limit our analysis to the 129 of 171 pointings that have been verified as having no significant systematic errors through a series of cosmology-insensitive systematic tests described in Heymans et al. (2012b).

This paper is organized as follows: in Section 2, we use a series of tests to determine whether the PDFs are sufficiently accurate to determine the redshift distributions for the many different science analyses of the CFHTLenS data set, and then apply our findings to the first tomographic analysis of the CFHTLenS data set in Section 3. We investigate the effect of non-linear modelling of the mass power spectrum and baryons on our tomographic weak lensing results in Section 4. Section 5 contains our concluding remarks.

2 GALAXY REDSHIFT DISTRIBUTIONS DETERMINED FROM THE PHOTOMETRIC REDSHIFT PDF

When considering the redshift of an individual galaxy, a best-fitting redshift must be measured from the PDF, typically corresponding to the peak of the PDF. If many galaxies are considered, the sum of their PDFs can be used as an estimate of the redshift distribution instead of the distribution of best-fitting redshifts. We show in this section that, by using information from the entire PDF, we achieve an accurate model of the redshift distribution. The accuracy of the PDFs is not known a priori since this depends on whether the template spectral energy distributions and prior information are a representative and complete description of the galaxies in the survey.

We compare the summed PDFs against several other methods of measuring the redshift distribution. These methods include a comparison with the overlapping VIMOS VLT Deep Survey (VVDS) and DEEP2 spectroscopic redshifts (see Section 2.1), statistical resampling of the CFHTLenS photometric redshifts using the COSMOS-30 redshifts (see Section 2.2) and a photometric redshift contamination analysis (see Section 2.3).

We divide the data into six redshift bins and measure the redshift distribution of each. We are limited in the total number of bins by the pairwise contamination analysis, which breaks down for larger numbers of bins (see Section 2.3 for a more detailed discussion). The redshifts are most reliable in the range $0.1 < z_{\rm p} < 1.3$ where comparison to spectroscopic redshifts, for $i' < 24.5$, shows the scatter to be $0.03 < \sigma_{\Delta z} < 0.06$, with an outlier rate of less than 10 per cent (Hildebrandt et al. 2012). Here $\sigma^2_{\Delta z}$ is the variance in the value of Δz, which is given by

$$\Delta z = \frac{z_{\rm p} - z_{\rm s}}{1 + z_{\rm s}}, \tag{1}$$

where $z_{\rm p}$ and $z_{\rm s}$ are the photometric and spectroscopic redshifts, respectively.

The redshift bins are chosen such that each bin is approximately four times wider than the photometric redshift error $0.04(1 + z_{\rm p})$. This is done to avoid excessive contamination between adjacent bins. For $z_{\rm p} > 1.3$, there are only a small number of galaxies, making a subdivision of this range difficult. The six bins are as follows:

Bin 1: $0.00 < z_1 \leq 0.17$
Bin 2: $0.17 < z_2 \leq 0.38$
Bin 3: $0.38 < z_3 \leq 0.62$
Bin 4: $0.62 < z_4 \leq 0.90$
Bin 5: $0.90 < z_5 \leq 1.30$
Bin 6: $1.30 < z_6$.

2.1 Comparison with spectroscopic redshifts

We begin by investigating the redshift distribution given by spectroscopic redshifts. Spectroscopic redshifts from the VVDS (Le Fèvre et al. 2005) and the DEEP2 galaxy redshift survey (Newman et al. 2012) overlap with CFHTLenS and were used to test the photometric redshifts. For a given photometric redshift bin, we can select those galaxies that have spectroscopic redshifts and examine their redshift distribution. The spectroscopic sample is complete for $i' \lesssim 22.0$, dropping to ∼90 per cent completeness for $i' < 23.0$. We adopt the latter cut to ensure that there are a sufficient number of galaxies for our analysis. The catalogues are also cut to exclude objects on masked regions and those that are flagged as stars. Stars are selected with `star_flag` (see Erben et al. 2012 for more details). Due to the dithering pattern, which ensures that exposures exist between individual CCD chips, there are a variable number of exposures over a single pointing. This changing photometric depth is difficult to account for when constructing a random catalogue with the same properties, which is necessary for the contamination analysis presented in Section 2.3. To avoid this complexity, a final cut is made to select galaxies on areas of the sky that were detected during every exposure, and random objects are placed only in these areas. We do not expect this to bias our results as there is no correlation between the physical properties of a galaxy and the part of the CCD mosaic it was observed on.

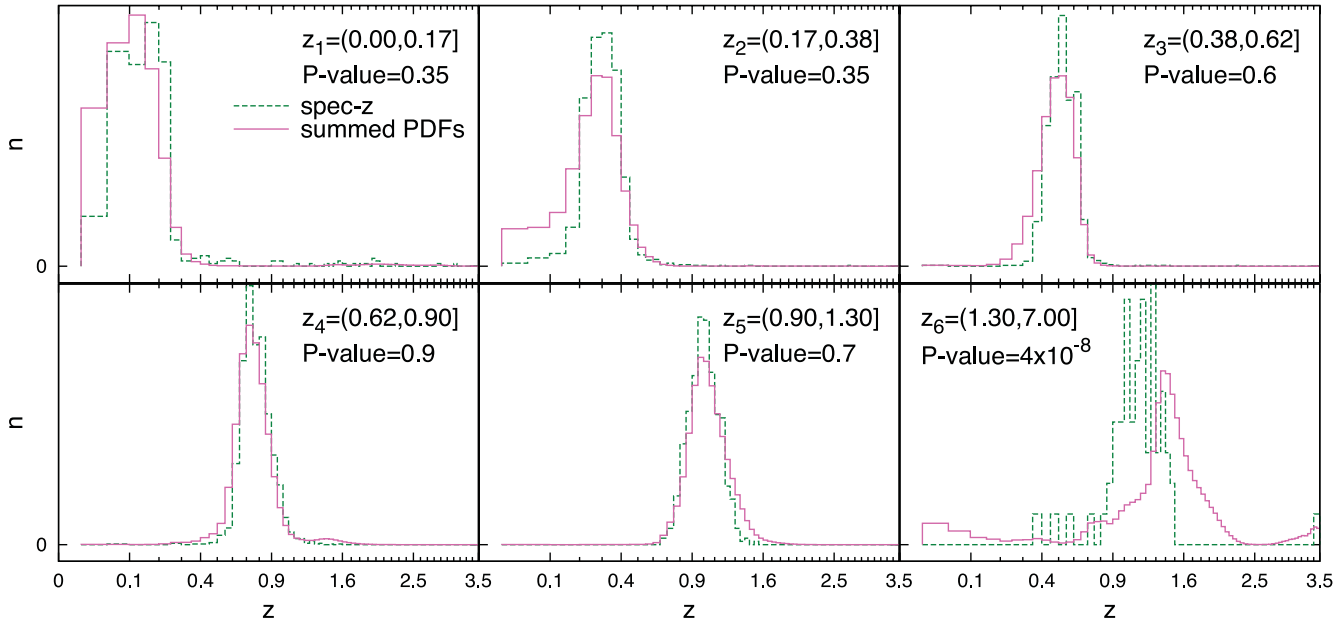

Figure 1. Comparison of the predicted redshift distributions within each broad redshift bin, labelled z_i. A magnitude cut of $i' < 23.0$ is used for comparison with spectroscopic redshifts. The solid lines (pink) show the summed PDFs for all galaxies within a given redshift bin. The dashed lines (green) show the spectroscopic redshift distribution. The listed *P*-values are the result of a two-sample Kolmogorov–Smirnov test of the distributions; we adopt a significance level of $\alpha = 0.05$ rejecting the null hypothesis that the two distributions are drawn from the same population for the highest redshift bin.

A comparison of redshift distributions for $i' < 23.0$ is presented in Fig. 1. For each redshift bin, we show the redshift distribution predicted by the summed PDF (solid line) and the spectroscopic redshift distribution (dashed line). The PDFs of all galaxies within a given redshift bin are summed and the resulting distribution normalized to obtain the solid line. If the summed PDF is a good representation of the true error distribution, then we would expect this distribution to agree with the redshift distribution measured with the spectroscopic redshifts.

We use the Kolmogorov–Smirnov two-sample test (KS test) to determine if the two distributions in Fig. 1 are consistent with being drawn from the same population (details of this test can be found in, for example, Wall & Jenkins 2003). Before performing the test, we adopt as a discriminating criterion a significance level of $\alpha = 0.05$. The *P*-values found from the KS test are presented as labels in Fig. 1. We find that the distributions for the first five redshift bins are consistent with having been drawn from the same population at a significance level of $\alpha = 0.05$. However, we can reject the null hypothesis for the last redshift bin at the same level of significance, indicating that the two distributions are significantly different. This is indicative of the large uncertainties in the photometric redshifts at $z_p > 1.3$ and confirms the choice of this cutoff made by Hildebrandt et al. (2012).

2.2 Comparison with COSMOS photometric redshifts

The agreement at bright magnitudes shown in Fig. 1 is encouraging. However, the majority of lensing studies include fainter galaxies; for example, a magnitude limit of $i' < 24.7$ is adopted for the measurement of CFHTLenS galaxy shapes (Miller et al. 2013). Therefore, we wish to investigate the redshift distribution with this deeper magnitude cut. The spectroscopic redshift sample described in Section 2.1 cannot be used for comparison since the completeness of this sample drops sharply beyond $i' \sim 23$. Instead, we use the COSMOS-30 photometric redshift catalogue (Ilbert et al. 2009), which is accurate to $\sigma_{\Delta z} \simeq 0.012$ due to 30 bands of wavelength coverage from the ultraviolet to the mid-infrared. Quoting values for the Subaru *i* band, the COSMOS-30 data are 99.8 per cent complete for $i < 25.5$, and have a 5σ point source limiting magnitude of $i \sim 26.2$ (Ilbert et al. 2009). A resampling procedure is used to estimate the redshift distribution of deep CFHTLenS galaxies based on the distribution of COSMOS-30 redshifts with CFHTLS overlap.

Although the $1.6\,\mathrm{deg}^2$ COSMOS field contains the $1\,\mathrm{deg}^2$ CFHTLS-Deep field D2, there are no overlapping CFHTLS-Wide fields. Therefore, it is not possible to directly match CFHTLenS galaxies to objects in the COSMOS-30 catalogue. This issue can be circumvented in a novel way using the photometric catalogue of D2 provided in Hildebrandt et al. (2009). Using the fact that the photometric systems for the CFHTLS-Wide and Deep data are identical, we add random Gaussian noise, scaled to simulate data taken at CFHTLS-Wide depth, to the multicolour magnitude estimates in the D2 photometric catalogue. Using artificially degraded catalogues generated in this way, we calculate a Wide-like photometric redshift estimate z_p using the maximum of the posterior distribution as described in Hildebrandt et al. (2012). This is done for each D2 object in a catalogue matched to the COSMOS-30 catalogue of Ilbert et al. (2009), employing an association radius of 1.0 arcsec. The COSMOS-30 redshifts in the matched catalogue are labelled z_{30}.

This matched catalogue of z_{30} and noise-degraded Wide-like z_p estimates can then be used to acquire information about the joint probability distribution of COSMOS-30 and CFHTLenS redshifts. We generate 100 realizations of the artificially degraded Wide-like catalogues, running the Bayesian photometric redshift estimation of Hildebrandt et al. (2012) for each realization. Using this ensemble of (z_{30}, z_p) pairs, we construct a two-dimensional histogram of galaxy number counts in square bins of width 0.0025 in redshift for both z_{30} and z_p. This histogram is then used as an empirical estimate of the conditional probability density function $P(z_{30}|z_p)$ and allows us to estimate the corresponding cumulative PDF $P(<z_{30}|z_p)$ for

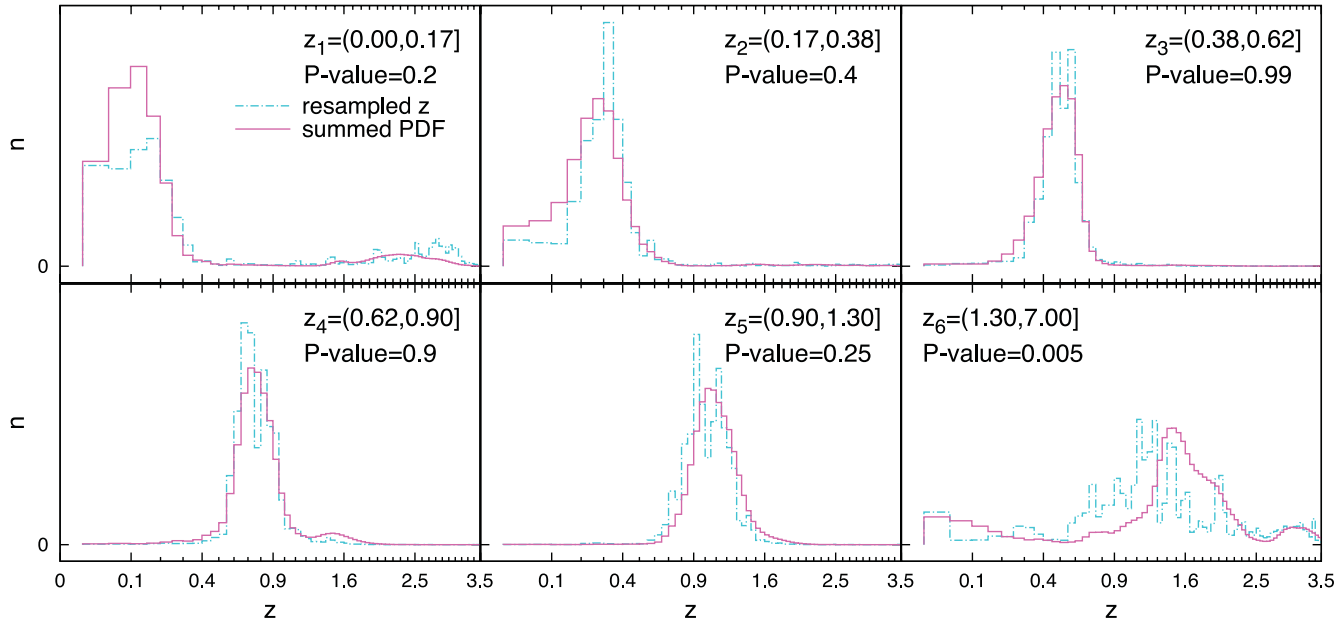

Figure 2. Comparison of the predicted redshift distributions with a magnitude cut of $i' < 24.7$. The solid lines (pink) show the summed PDFs for all galaxies within a given redshift bin. The dot–dashed histogram (cyan) shows the result of resampling the CFHTLenS redshifts using the constructed conditional probability $P(z_{30}|z_p)$. The P-values are the result of a KS test; we reject the null hypothesis for the highest redshift bin at $\alpha = 0.05$.

each z_p bin. Then, using inversion sampling from $P(<z_{30}|z_p)$ with a uniform pseudo-random number generator, samples of redshifts distributed according to $P(z_{30}|z_p)$ can be drawn.

With the assumption that $P(z_{true}|z_p) = P(z_{30}|z_p)$, the contamination in tomographic redshift bins can be estimated by resampling CFHTLenS redshifts according to $P(z_{30}|z_p)$. The resulting redshift distributions predicted from this method are given as dot–dashed lines in Fig. 2, and the summed PDFs are presented as solid lines. Note that the fine structure seen in the resampled redshifts is due to structures in the COSMOS field and does not represent real structures in the distribution of CFHTLenS galaxies. The small size of COSMOS means that it is limited by sample variance, and individual clusters are able to leave an imprint on the resampled galaxies. This only affects the fine details of the resampled redshifts leading to a breakdown of the assumption that $P(z_{true}|z_p) = P(z_{30}|z_p)$ for small redshift intervals.

We again adopt the null hypothesis that the two distributions are drawn from the same population. Using a KS test we find that the null hypothesis can be rejected at a significance level of $\alpha = 0.05$ for the $z_p > 1.3$ redshift bin, but not for any of the other bins. The P-values found from the KS test are presented as labels in Fig. 2. Our results again confirm that the CFHTLenS photometric redshifts of the $z_p > 1.3$ galaxies are unreliable. However, we find no evidence that the galaxies at $z_p < 0.1$, which is the lower limit for the high-confidence redshift range (Hildebrandt et al. 2012), are unreliable. This is likely because our lowest redshift bin extends to $z_p = 0.17$ and is therefore dominated by galaxies with well-measured photometric redshifts.

2.3 Redshift contamination from angular correlation functions

In order to further test the accuracy of the photometric redshift PDFs, we measure the redshift contamination using an angular cross-correlation technique (Benjamin et al. 2010). This method has few assumptions and is sensitive to any contamination between redshift bins. Since it only relies on the angular correlation function of the galaxies, it is independent of the other methods used and serves as a critical test.

2.3.1 *Overview of method*

Galaxies cluster in overdense regions, leading to an excess in the number of pairs found at a separation θ when compared to a random distribution of points. The two-point angular correlation function $\omega(\theta)$ quantifies this excess probability of finding pairs. A common estimator (Landy & Szalay 1993) is

$$\omega_{ij} = \frac{(D_i D_j)_\theta}{(RR)_\theta}\frac{N_R N_R}{N_i N_j} - \frac{(D_i R)_\theta}{(RR)_\theta}\frac{N_R}{N_i} - \frac{(D_j R)_\theta}{(RR)_\theta}\frac{N_R}{N_j} + 1, \qquad (2)$$

where $(D_iD_j)_\theta$ is the number of pairs separated by a distance θ between data sets i and j, $(RR)_\theta$ is the number of pairs separated by a distance θ for a random set of points, $(D_iR)_\theta$ is the number of pairs separated by a distance θ between data set i and a random set of points, N_R is the number of points in the random sample and N_i (N_j) is the number of points in data sample i (j). The autocorrelation is described by the case $i = j$, and the cross-correlation by the case $i \neq j$. Our analysis would hold for any estimator of the angular correlation function.

In the Λ cold dark matter (CDM) model, galaxies in well-separated non-overlapping redshift bins are not significantly clustered with each other. Therefore, clustering between these bins should be consistent with a random distribution of points, resulting in $\omega_{ij} = 0$. Adjacent redshift bins will have a small positive ω_{ij} owing to galaxy clustering at their shared edge, which becomes more pronounced for narrow redshift bins. If any non-zero angular cross-correlation is detected between the photometric redshift bins, they must share galaxies with similar redshifts.

As shown in Benjamin et al. (2010), this simple realization can be exploited to estimate contamination between photometric redshift bins. The reader is referred to that work for the full details of the

method. Here we present only a few key equations and concepts before we apply the method to the CFHTLenS data.

The contamination fraction, f_{ij}, is defined as the number of galaxies contaminating bin j from bin i as a fraction of the total number of galaxies $N_i^{\rm T}$ which have a spectroscopic redshift that lies within redshift bin i. If there is no overlap or contamination between redshift bins, $f_{ij} = 0$ when $i \neq j$, and $N_i^{\rm T} = N_i^{\rm o}$, where $N_i^{\rm o}$ is the total number of galaxies which have a photometric redshift that lies within redshift bin i. In the standard case of overlapping photometric redshift bins, the contamination fraction relates the observed number of galaxies in each photometric redshift bin $N_i^{\rm o}$ to the true underlying number of galaxies $N_i^{\rm T}$ as follows:

$$\begin{pmatrix} N_1^{\rm o} \\ N_2^{\rm o} \\ \cdots \\ N_m^{\rm o} \end{pmatrix} = \begin{pmatrix} f_{11} & f_{21} & \cdots & f_{m1} \\ f_{12} & f_{22} & \cdots & f_{m2} \\ \cdots & \cdots & \cdots & \cdots \\ f_{1m} & f_{2m} & \cdots & f_{mm} \end{pmatrix} \begin{pmatrix} N_1^{\rm T} \\ N_2^{\rm T} \\ \cdots \\ N_m^{\rm T} \end{pmatrix}, \tag{3}$$

where m is the number of redshift bins and $f_{ii} = 1 - \sum_{k \neq i}^{m} f_{ik}$. We determine the contamination fractions f_{ij} from measurements of $\omega_{ij}^{\rm o}$, the observed two-point correlation function between photometric redshift bins i and j. For two redshift bins, it can be shown that

$$\omega_{12}^{\rm o} = \frac{\omega_{11}^{\rm o} \left(\frac{N_1^{\rm o}}{N_2^{\rm o}}\right) f_{12}(1 - f_{21}) + \omega_{22}^{\rm o} \left(\frac{N_2^{\rm o}}{N_1^{\rm o}}\right) f_{21}(1 - f_{12})}{(1 - f_{12})(1 - f_{21}) + f_{12} f_{21}}. \tag{4}$$

Since $\omega_{12}^{\rm o}$ is measured at multiple angular scales, it is possible to determine the contamination fractions f_{12} and f_{21}. Degeneracy exists between f_{12} and f_{21}, which can be broken if the angular autocorrelation functions $\omega_{11}^{\rm o}$ and $\omega_{22}^{\rm o}$ have significantly different shapes. We expect this to be the case for the angular correlation functions of galaxy samples at different redshifts.

When considering more than two redshift bins, we measure the contamination fractions using equation (4) for each pair of bins in turn. This pairwise approximation assumes that higher order contamination can be safely ignored, that is, the angular cross-correlation is not affected by the mutual contamination of the pair of bins by another redshift bin. As the number of bins increases or if the contamination fractions become large, this assumption is no longer valid and the method breaks down.

Once the contamination fractions f_{ij} have been measured, we can invert[2] the contamination matrix in equation (3) to determine the true underlying number of galaxies in each redshift range $N_i^{\rm T}$ from the observed number of galaxies in each photometric redshift bin $N_i^{\rm o}$. The true redshift distribution $n^i(z_j)$ for each photometric redshift bin i is then calculated over the full redshift range, sampled at each redshift z_j from

$$n^i(z_j) = f_{ij} N_i^{\rm T}. \tag{5}$$

2.3.2 Contamination analysis

In order to estimate the contamination fractions in the CFHTLenS data, the angular correlation functions must be measured. Brute-force pair counting algorithms are $\mathcal{O}(N^2)$, where N is the number of galaxies, which for our data set results in prohibitively large computation times. The publicly available code ATHENA[3] employs a tree data structure to increase the speed of pair counting to $\mathcal{O}(N \log(N))$ at the cost of accuracy. The level of approximation is parametrized by the opening angle. Larger values indicate larger approximations with an opening angle of zero representing no approximation. Galaxies are grouped together into nodes in the tree data structure based on angular position. The structure is a hierarchy with the nodes on top containing more galaxies. The opening angle determines when to descend to lower nodes and higher spatial resolution. Tests of ATHENA against a more simplistic and robust algorithm are used to determine that with an opening angle of 0.03 we make at most a 1 per cent error on the angular correlation function. This value of opening angle is used when measuring the angular correlation function.

For each pointing we measure the angular correlation function in six angular bins spaced logarithmically in the range $0.15 < \theta < 30$ arcmin. Above 30 arcmin, the signal is very small providing little additional information. For each pointing, the contamination fractions are estimated via the angular correlation function as outlined in Section 2.3.1. The covariance is estimated via a bootstrap technique, with an additional contribution coming from the field-to-field variance for the angular cross-correlations. The details of the maximum likelihood technique and covariance matrix are presented in appendix A of Benjamin et al. (2010). The likelihoods for the contamination fractions from each field are then combined with equal weighting.

The following matrices contain the measured contamination fractions with 68 per cent confidence regions. All values are multiplied by 100 for ease of viewing. For the bright sample, $i' < 23.0$, we find

$$f_{ij} = \begin{pmatrix} 65 \pm 5 & 4 \pm 1 & < 1 & < 1 & < 1 & 6 \pm 6 \\ 28 \pm 4 & 87 \pm 3 & 8 \pm 2 & < 1 & < 1 & 7 \pm 7 \\ 1 \pm 1 & 7 \pm 2 & 85 \pm 3 & 9 \pm 2 & 1 \pm 1 & 7 \pm 7 \\ 1 \pm 1 & < 1 & 6 \pm 2 & 85 \pm 2 & 38 \pm 6 & 5 \pm 5 \\ < 1 & < 1 & < 1 & 4 \pm 1 & 56 \pm 7 & 29 \pm 12 \\ 3 \pm 1 & < 1 & < 1 & < 1 & 3 \pm 1 & 18 \pm 16 \end{pmatrix}. \tag{6}$$

With a cut of $i' < 24.7$, we measure

$$f_{ij} = \begin{pmatrix} 42 \pm 8 & 3 \pm 2 & < 1 & 1 \pm 1 & < 1 & 9 \pm 6 \\ 32 \pm 4 & 75 \pm 3 & 8 \pm 2 & < 1 & < 1 & 1 \pm 1 \\ < 1 & 18 \pm 2 & 79 \pm 3 & 7 \pm 2 & < 1 & 1 \pm 1 \\ 4 \pm 4 & < 1 & 11 \pm 2 & 78 \pm 3 & 20 \pm 3 & 3 \pm 3 \\ < 1 & < 1 & < 1 & 9 \pm 2 & 73 \pm 4 & 42 \pm 5 \\ 18 \pm 4 & 2 \pm 1 & < 1 & 4 \pm 1 & 5 \pm 3 & 36 \pm 6 \end{pmatrix}. \tag{7}$$

Many of the contamination fractions are 1 per cent deviations from zero, which is expected since we have this level of uncertainty in our estimation of the angular correlation functions. Note that the ith column contains the location of all bin i galaxies. Due to the pairwise treatment of redshift bins, columns do not sum to exactly 100 per cent. These matrices are extremely well conditioned with condition numbers of 8.72 and 6.35 for the $i' < 23.0$ and $i' < 24.7$ cases, respectively, indicating that matrix inversion is

[2] Since we expect the non-diagonal contamination fractions to be small, the matrix should be diagonally dominant and therefore invertible.
[3] http://www2.iap.fr/users/kilbinge/athena/

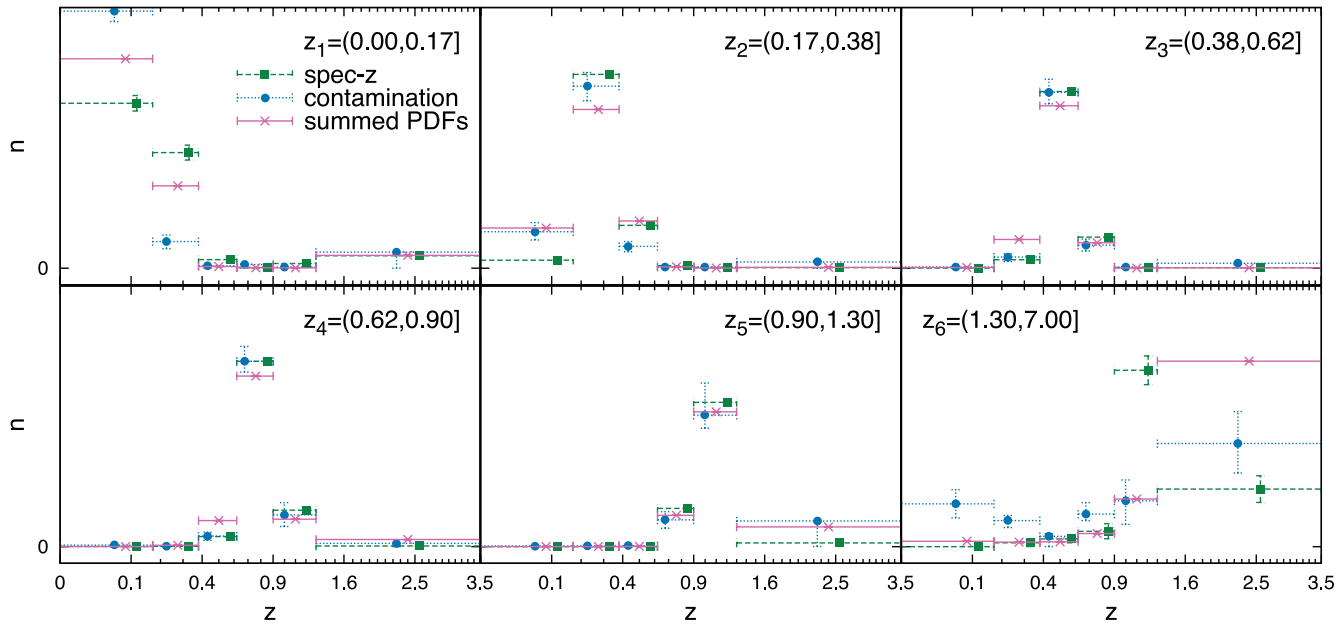

Figure 3. Comparison of the predicted true redshift distribution within each broad redshift bin, labelled z_i. A magnitude cut of $i' < 23.0$ is used for comparison with spectroscopic redshifts. All horizontal error bars denote the width of the redshift bin and points are offset horizontally for clarity. The crosses with solid lines (pink) denote the summed PDFs when integrated within a given broad redshift bin; the error is calculated as the standard deviation from 1000 bootstrap samples. The filled circles with dotted lines (blue) show the result from our contamination analysis with 68 per cent confidence region. The filled squares with dashed lines (green) show the spectroscopic redshift data integrated within each broad redshift bin. The error is the standard deviation of 1000 bootstrap samples.

numerically stable and does not contribute a significant uncertainty to the solution of equation (3).

With the contamination fractions measured, the true number of galaxies in each redshift bin can be calculated from equation (3). The redshift distribution is then found from equation (5). This is done with a Monte Carlo procedure for finding global solutions to the contamination matrix presented in Benjamin et al. (2010). We can now compare our contamination results with those found from the spectroscopic redshifts and the COSMOS-30 photometric redshifts. However, since our contamination results exist in only six redshift bins, we must also sum the distributions shown in Figs 1 and 2 within these six redshift bins.

For $i' < 23.0$, we present our contamination results in Fig. 3. For each redshift bin we show the redshift distribution predicted by the PDFs (crosses with solid lines), the contamination analysis (filled circles with dotted lines) and the spectroscopic redshift distribution (filled squares with dashed lines). The horizontal error bars on all points denote the width of the redshift bins. The vertical scale is proportional to the number of galaxies but uses arbitrary units. For the summed PDF, the vertical error bar is calculated as the standard deviation of the summed PDFs for 1000 bootstraps of the galaxies within each bin z_i. Note that given the large number of galaxies in each bin ($\sim$40 000$-$600 000), the statistical error of the summed PDF is very small. The vertical error bars on the contamination results enclose the 68 per cent confidence region which comes from a procedure for finding global solutions to the contamination (Benjamin et al. 2010). The vertical error on the spectroscopic redshift distribution is taken as the standard deviation from 1000 bootstraps of the spectroscopic catalogue. For both cases where bootstraps are used, we verified that 1000 bootstraps yield stable error estimates. For each bootstrap, objects are sampled with replacement and the resulting redshift distributions measured; the total number of galaxies sampled is equal to the number in the original catalogues.

Fig. 3 shows the predicted redshift distribution for each of the six redshift bins used. The contamination points for a given subplot are contained within the corresponding row of the contamination matrix in equation (6). For example, the top row shows that the majority of galaxies from bin 1 remain in bin 1, with $f_{11} = 65 \pm 5$ per cent. Contamination from other bins is less than the per cent level except for the neighbouring bin with $f_{21} = 4 \pm 1$ per cent and the highest redshift bin with $f_{61} = 6 \pm 6$. Keep in mind that the relative heights of points in the z_1 subplot do not follow these contamination values because the contamination f_{ij} represents the number of galaxies in bin j from bin i divided by the true number in bin i. However, investigating the matrix in relation to Fig. 3 can help in grasping the presented information. We expect that the spectroscopic redshift distribution is the true distribution, assuming that the limited area of the spectroscopic samples does not bias the results, which is a reasonable assumption for our purposes. The contamination model is in poor agreement with the spectroscopic sample in the z_1 and z_6 subplots. For z_1, the contamination model underpredicts the contamination from bin 2 to bin 1, underestimating f_{21} as evidenced by the discrepancy between the contamination point and the spectroscopic point in the second bin of the z_1 subplot. Similarly, the contamination is overpredicted for f_{12} which is seen in the first bin of the z_2 subplot. This represents a fundamental degeneracy in the angular cross-correlation method. Although an angular cross-correlation is detected between these two bins, unless the angular autocorrelations have significantly different slopes, the method cannot distinguish easily between bin 1 galaxies contaminating bin 2 or vice versa. A similar degeneracy explains the discrepancies in the z_6 subplot; there we see that f_{56} predicted by the angular cross-correlation is too low and f_{65} in the z_5 subplot is

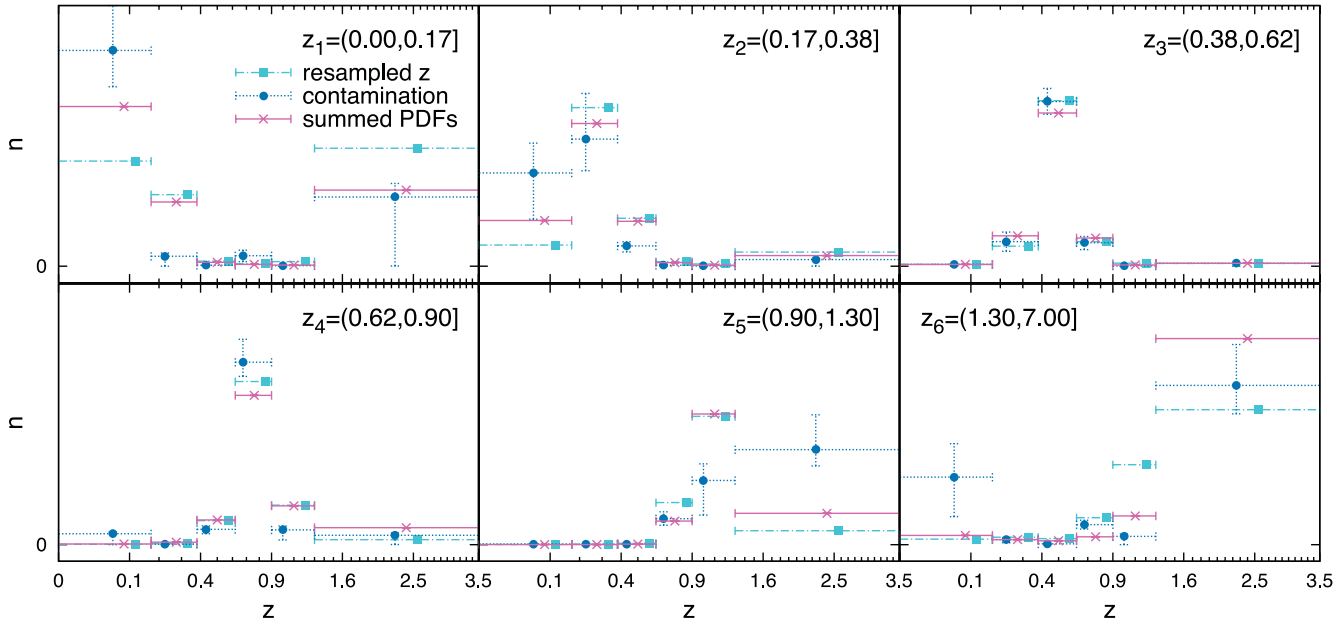

Figure 4. Same as Fig. 3 except for the following differences. A magnitude cut of $i' < 24.7$ is used. The filled squares with dot–dashed lines (cyan) show the resampled COSMOS-30 data integrated within each broad redshift bin. The error is given as the standard deviation of the 100 low-resolution reconstructions (see Section 2.2).

too high. The contamination between these bins is detected but the direction of scatter is misidentified.

We use a KS test to determine if the distributions in Fig. 3 are consistent with being drawn from the same population. Since there are three distributions and the KS test is a two-sample test, we apply it to each pair of distributions. Furthermore, due to the small number of bins we must rely on tabulated critical values which exist for a very few significance levels; therefore, we are not able to list the *P*-values for each redshift bin. For each pair of distributions, we find that we cannot reject the null hypothesis (drawn from the same population) at a significance level of $\alpha = 0.05$ for any of the redshift bins.

We present the results of the contamination analysis for $i' < 24.7$ in Fig. 4. The summed PDF and contamination results are presented similarly to Fig. 3. The resampled redshifts using COSMOS-30 are given as the dot–dashed lines and filled squares. The vertical error on the COSMOS-30 points is taken as the standard deviation of the 100 low-resolution resamplings (see Section 2.2). If we compare the contamination results to the resampled redshifts, the greatest discrepancies are for the z_1, z_5 and z_6 subplots. The $f_{12} - f_{21}$ and $f_{56} - f_{65}$ degeneracies noted for the bright sample above appear again in Fig. 4. Additionally, the resampled redshifts predict a larger f_{61} and smaller f_{16} than do the contamination results which can be seen in the first and last bins of the z_1 and z_6 subplots, respectively. The contamination analysis predicts that a significantly lower number of galaxies belong to bin 5 compared to the other methods; see bin 5 of the z_5 subplot. However, this is not due to scattering of bin 5 galaxies elsewhere, note that $f_{55} = 73 \pm 4$ per cent; instead the contamination analysis simply predicts fewer galaxies occupying this bin. To determine if these differences are statistically significant, we use a KS test. We again have three distributions and apply the test between each pair. For each pair of distributions, we find that we cannot reject the null hypothesis (drawn from the same population) at a significance level of $\alpha = 0.05$ for any of the redshift bins.

When using the finely binned spectroscopic and resampled redshifts in Sections 2.1 and 2.2, we were able to reject the null hypothesis for the high-redshift bin $z_p > 1.3$. The smallest *P*-value found was in the high-redshift bin when comparing the summed PDF with the spectroscopic distribution in Fig. 1. Performing the same comparison with these distributions when summed within the six redshift bins of the contamination analysis, we are not able to reject the null hypothesis. The coarse binning required by the contamination analysis has reduced the statistical power of the test. However, the contamination analysis provides a complementary estimation of the redshift distribution, which agrees well with the other estimates and strengthens our confidence in the summed PDF as an accurate measure of the redshift distribution.

We conclude that the summed PDF can be used to estimate the redshift distribution for the high-confidence redshift range $0.1 < z_p < 1.3$ determined by Hildebrandt et al. (2012). The comparison with the resampled COSMO-30 redshifts and the contamination analysis for $i' < 24.7$ suggest that an accurate estimate of the redshift distribution, including statistical and catastrophic errors, can be obtained from the sum of the PDFs. This result suggests that the model galaxy spectra and priors used in Hildebrandt et al. (2012) are a fair and sufficiently complete representation for the population of galaxies studied here.

3 WEAK LENSING TOMOGRAPHY

In this paper, we present an analysis of the CFHTLenS tomographic weak lensing signal using two broad redshift bins and compare our results with a 2D analysis over the same redshift range. Setting our analysis in a flat ΛCDM cosmology framework, the initial aim is to use the consistent results we find between successive tomographic bins as a demonstration that the CFHTLenS catalogues are not subject to the redshift-dependent systematic biases that were uncovered in an earlier analysis of CFHTLS data (Kilbinger et al. 2009). This

cosmology-dependent demonstration is the last in an extensive series of tests, which investigate the robustness and accuracy of the CFHTLenS catalogues. We stress, however, that this analysis was performed after the conclusion of a series of cosmology-insensitive tests presented in Heymans et al. (2012b) and the photometric redshift accuracy analysis presented in Section 2. Most importantly, no feedback loop existed between this cosmology-dependent test and the systematics and image simulation tests that determined the calibration corrections and the subset of reliable data that we use from the survey.

We choose to use two broad mid- to high-redshift bins for our tomographic analysis in order to reduce the potential contamination to the signal from intrinsic galaxy alignments (see, for example, Heavens et al. 2000; Heymans et al. 2012a, and references therein). We estimate the expected contamination of the measured weak lensing signal using the linear tidal field intrinsic alignment model of Hirata & Seljak (2004) and following Bridle & King (2007) by fixing its amplitude to the observational constraints obtained by Brown et al. (2002). By limiting the redshift bins to photometric redshifts $0.5 < z_{\rm p} \leq 0.85$ and $0.85 < z_{\rm p} \leq 1.3$, we estimate that any contamination from intrinsic alignments is expected to be no more than a few per cent for each redshift bin combination. We therefore ignore any contributions from intrinsic alignments in this analysis as they are expected to be small in comparison to our statistical errors. Note that a low level of contamination would not be expected if we instead used the six narrow redshift bins that were analysed in the redshift contamination analysis in Section 2. We present a fine six-bin tomographic analysis of the data in Heymans et al. (2012a) where the impact of intrinsic galaxy alignments is mitigated via the simultaneous fit of a cosmological model and an intrinsic alignment model. The findings of Heymans et al. (2012a) support the approach taken in this paper to neglect the contribution of intrinsic alignments for our choice of redshift bins.

The 2D lensing analysis presented here is restricted to the same redshift range used in our tomographic analysis $0.5 < z_{\rm p} \leq 1.3$. We measure the shear correlation function on angular scales from $\sim$1 to $\sim$40 arcmin. The upper limit is set by our ability to measure the covariance matrix from simulations, see Section 3.3.1.

3.1 Overview of tomographic weak lensing theory

The complex weak lensing shear $\gamma = \gamma_1 + {\rm i}\gamma_2$, which is directly analogous to the complex galaxy ellipticity, can be decomposed into two components: the tangential shear $\gamma_{\rm t}$ and the cross component $\gamma_{\rm x}$. These are defined relative to the separation vector for each pair of galaxies, with $\gamma_{\rm t}$ describing elongation and compression of the ellipticity along the separation vector and $\gamma_{\rm x}$ describing elongation and compression along a direction rotated 45° from the separation vector. The following shear–shear correlation functions can then be computed:

$$\xi_{\pm}^{k,l}(\theta) = \frac{\Sigma_{i,j}\left[\gamma_{t,i}^{k}(\boldsymbol{\vartheta}_i)\gamma_{t,j}^{l}(\boldsymbol{\vartheta}_j) \pm \gamma_{x,i}^{k}(\boldsymbol{\vartheta}_i)\gamma_{x,j}^{l}(\boldsymbol{\vartheta}_j)\right] w_i w_j \Delta_{ij}}{\Sigma_{i,j} w_i w_j \Delta_{ij}}, \quad (8)$$

where galaxy pairs labelled i,j are separated by angular distance $\vartheta = |\boldsymbol{\vartheta}_i - \boldsymbol{\vartheta}_j|$. If ϑ falls in the angular bin given by θ, then $\Delta_{ij} = 1$, otherwise $\Delta_{ij} = 0$. The labels k,l identify redshift bins. The summation is performed for all galaxies i in bin k and all galaxies j in bin l. The contribution of each galaxy pair is weighted by its inverse variance weight $w_i w_j$. This gives greater significance to galaxy pairs with well-measured shapes.

Shear calibration is performed as described in Miller et al. (2013) and Heymans et al. (2012b). This signal-to-noise (S/N) and size-dependent calibration include an additive (c) and a multiplicative (m) correction term as follows:

$$\gamma^{\rm obs} = (1+m)\gamma^{\rm true} + c. \quad (9)$$

An average additive correction of 2×10^{-3} is found for γ_2. The additive correction for γ_1 is found to be consistent with zero. The multiplicative correction to $\xi_{\pm}$ is found by calculating the weighted correlation function of $1 + m$ (Miller et al. 2013),

$$1 + K^{k,l}(\theta) = \frac{\Sigma_{i,j}(1+m_i^k)(1+m_j^l) w_i w_j \Delta_{ij}}{\Sigma_{i,j} w_i w_j \Delta_{ij}}. \quad (10)$$

The shear correlation functions $\xi_{\pm}$ are then corrected by dividing them by $1 + K$.

The shear–shear correlations can also be expressed as filtered functions of the convergence power spectra

$$\xi_{+/-}^{k,l}(\theta) = \frac{1}{2\pi}\int_0^{\infty} {\rm d}\ell\, \ell\, J_{0/4}(\ell\theta) P_{\kappa}^{k,l}(\ell), \quad (11)$$

where J_n is the nth order Bessel function of the first kind and ℓ is the modulus of the two-dimensional wavevector. These can be related to line-of-sight integrals of the three-dimensional matter power spectrum

$$P_{\kappa}^{k,l}(\ell) = \frac{9\, H_0^4\, \Omega_{\rm m}^2}{4c^4}\int_0^{\chi_{\rm h}} {\rm d}\chi\, \frac{g_k(\chi) g_l(\chi)}{a^2(\chi)} P_{\delta}\left(\frac{\ell}{f_K(\chi)}, \chi\right), \quad (12)$$

where c is the speed of light, $\Omega_{\rm m}$ is the matter energy density, H_0 is the Hubble constant, $f_K(\chi)$ is the comoving angular diameter distance out to a distance χ, $\chi_{\rm h}$ is the comoving horizon distance, $a(\chi)$ is the scale factor and P_{δ} is the three-dimensional mass power spectrum computed from a non-linear estimation of dark matter clustering (Smith et al. 2003). The two terms, $g_k(\chi)$, are the geometric lens efficiency, which depend on the redshift distribution of the sources, $n_k(\chi')$,

$$g_k(\chi) = \int_{\chi}^{\chi_{\rm h}} {\rm d}\chi' n_k(\chi') \frac{f_K(\chi' - \chi)}{f_K(\chi')}. \quad (13)$$

Given a cosmological model, matter power spectrum and redshift distribution of the sources, we can model the shear correlation functions. Bayesian model-fitting techniques are then used to obtain the posterior probability on the model vector given the observed shear correlation functions. We discuss this further in Section 3.3.

3.2 The tomographic weak lensing signal

Based on the results presented in Section 2, the redshift distribution in each bin is taken to be the sum of the PDFs determined from the photometric redshift analysis of Hildebrandt et al. (2012). We refer to the maximum posterior photometric redshift estimate as the 'photometric redshift'. The histogram of photometric redshifts and the sum of the PDFs for each redshift bin are presented in Fig. 5. Note that the summed PDFs extend to lower and higher redshifts than the photometric redshifts do, broadening the range below $z = 0.5$ and above $z = 1.3$. The summed PDFs for the two redshift bins also overlap considerably with one another. The average redshift from the summed PDFs is 0.7 for the low-redshift bin and 1.05 for the high-redshift bin. For the photometric redshifts, we find 0.69 and 1.03 for the low- and high-redshift bins, respectively. The average redshift for both bins taken together is found to be 0.87 from the summed PDFs and 0.84 from the photometric redshifts.

We use ATHENA with an opening angle of 0.02 to measure the shear–shear correlation function. We have tested that the difference to the shear–shear correlation function when using an opening

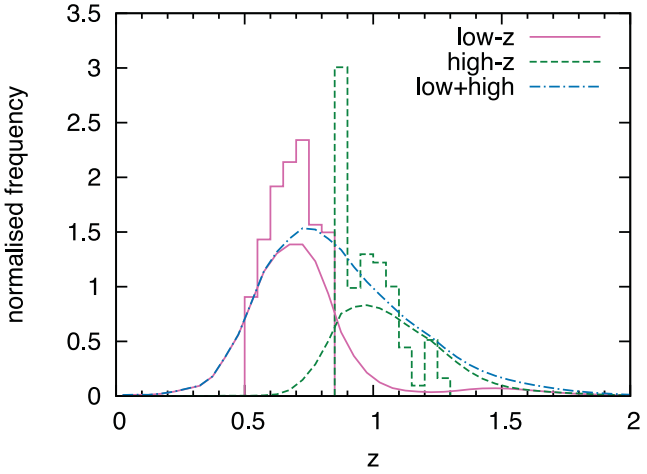

Figure 5. Redshift distributions used in the weak lensing analysis. Low- and high-redshift bins correspond to $z_p = (0.5, 0.85]$ and $(0.85, 1.3]$, respectively. The smooth curves show the result of summing the photometric redshift PDFs of all galaxies within the respective redshift bin. The smooth solid and dashed curves are used in the tomographic analysis and the sum of the PDFs over the entire redshift range is given by the smooth dot–dashed line which is used in the 2D lensing analysis. For comparison, the histograms show the redshift distribution obtained from the photometric redshifts.

angle of 0.02 compared to a brute-force calculation is negligible, approximately 8 per cent of the size of the errors. The signal is first measured on each of the four wide mosaics: W1, W2, W3 and W4, applying the shear calibration described in Section 3.1. The correlation functions are then combined by calculating the weighted average. The weight for a given angular bin and wide mosaic is the sum of the inverse variance weight terms for each pair of galaxies. We present ξ_+ and ξ_- for each redshift bin combination in Fig. 6. The error bars correspond to the diagonal elements from the covariance matrix, discussed in more detail in Section 3.3.1. The lines denote the theoretical prediction for a fiducial cosmological model using *Wilkinson Microwave Anisotropy Probe* '7-year (*WMAP*7) best-fitting results (Komatsu et al. 2011); hence, the following parameter vector is used: ($\Omega_m = 0.271$, $\sigma_8 = 0.78$, $h = 0.704$, $\Omega_b = 0.0455$, $n_s = 0.967$, $\Omega_\Lambda = 0.729$, $w_0 = -1$). Descriptions of each parameter can be found in Table 1. To compute the theoretical models we employ the halo model of Smith et al. (2003) to estimate the non-linear matter power spectrum and the analytical approximation of Eisenstein & Hu (1998) to estimate the transfer function.

Emphasizing that no cosmology-dependent systematic tests were used to vet the catalogues (Heymans et al. 2012b), Fig. 6 demonstrates the robustness of the CFHTLenS catalogues. The tomographic shear signal shows no evidence of a redshift-dependent bias as was seen in earlier CFHTLS data analyses (Kilbinger et al. 2009). We discuss further tests of the redshift scaling of the shear in Section 3.3.3.

3.3 Cosmology

From the signal measured in Section 3.2, cosmological parameters are estimated using COSMOPMC. COSMOPMC is a freely available[4] Population Monte Carlo (PMC) code, which uses adaptive importance sampling to explore the posterior likelihood (Kilbinger et al. 2011). COSMOPMC documentation can be found in Kilbinger et al. (2011);

[4] http://cosmopmc.info

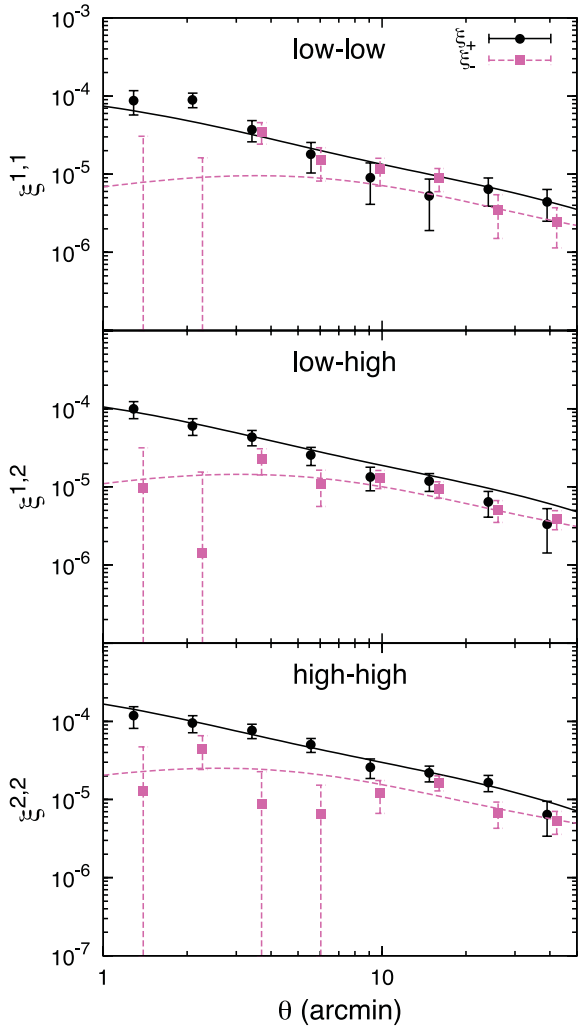

Figure 6. The filled circles with solid lines and filled squares with dashed lines show the measured signal for ξ_+ and ξ_-, respectively. Each panel shows the shear correlation functions for a unique pairing of redshift bins. The top, middle and bottom panels correspond to low redshift correlated with low redshift (low–low), low with high redshift (low–high) and high with high redshift (high–high). Error bars are the square root of the diagonal of the covariance matrix measured from mock catalogues (see Section 3.3.1). Theoretical predictions for a fiducial (*WMAP*7; Komatsu et al. 2011) cosmology are presented as lines; these are not the best-fitting models. There are two negative data points for ξ_- in the top panel; their values are -2.3×10^{-6} and -4.9×10^{-6} for scales 1.34 and 2.18 arcmin, respectively.

discussion of Bayesian evidence and examples of its application to various cosmological data sets can be found in Kilbinger et al. (2010) and Wraith et al. (2009). The PMC method is detailed in Cappé et al. (2007). The non-linear matter power spectrum is estimated using the halo model of Smith et al. (2003). The transfer function is estimated using the analytical approximation of Eisenstein & Hu (1998).

We explore two cosmologies: a flat ΛCDM universe and a curved ΛCDM universe. The model-dependent data vector used with COSMOPMC contains the following seven parameters: (Ω_m, σ_8, h, Ω_b, n_s, Ω_Λ, w_0). Physical descriptions and priors are presented in Table 1. For the flat ΛCDM model we have a five-parameter fit, where we fix $\Omega_\Lambda = 1 - \Omega_m$ and $w_0 = -1$. For the curved ΛCDM model we have six free parameters as Ω_Λ is allowed to vary, while w_0 remains fixed.

Table 1. Details of the model-dependent cosmological parameters for each of the considered cosmologies. Parameter ranges denote hard priors. A flat distribution is used throughout the range. The bottom three parameters are constrained by *WMAP*7 and are required in order to deduce σ_8.

Parameter	Flat ΛCDM	Curved ΛCDM	Description
Ω_m	[0, 1.0]	[0, 1.2]	Energy density of matter (baryons+dark matter).
σ_8	[0.2, 1.5]	[0.2, 1.5]	Normalization of the matter power spectrum.
h	[0.4, 1.2]	[0.4, 1.2]	The dimensionless Hubble constant $h = \frac{H_0}{100\,\mathrm{km\,s^{-1}\,Mpc^{-1}}}$.
Ω_b	[0, 0.1]	[0, 0.1]	Energy density of baryons.
n_s	[0.7, 1.3]	[0.7, 1.3]	Slope of the primordial matter power spectrum.
Ω_Λ	$1-\Omega_m$	[0, 2]	Energy density of dark energy.
w_0	-1	-1	Constant term in the dark energy equation of state, $w(a) = w_0$.
τ	[0.04, 0.20]	[0.04, 0.20]	Reionization optical depth.
$\Delta^2_{\mathcal{R}}$	[1.8, 3.5]	[1.8, 3.5]	Amplitude of curvature perturbations, units of 10^{-9} times the amplitude of density fluctuations.
A_{SZ}	[0.0, 2.0]	[0.0, 2.0]	Sunyaev–Zel'dovich template amplitude.

Three other cosmological data sets are used to provide complementary constraining power. Constraints from the cosmic microwave background (CMB) are taken from the seven-year results of *WMAP* (Komatsu et al. 2011, hereafter referred to as *WMAP*7). To obtain parameter constraints we use the publicly released *WMAP* likelihood code. Baryon acoustic oscillation (BAO) data are taken from the BOSS experiment (Anderson et al. 2012, hereafter referred to as BOSS). We consider the ratio $D_V/r_s = 13.67 \pm 0.22$ of the apparent BAO at $z = 0.57$ to the sound horizon distance to be Gaussian distributed. The Hubble constant is constrained with the results from the *Hubble Space Telescope* distance ladder (Riess et al. 2011, hereafter referred to as R11). Following R11, we use a Gaussian prior of mean value $h = 0.738$ and standard deviation $\sigma = 0.024$. For more details of these data sets, see Kilbinger et al. (2013). With *WMAP*7 the parameter set is expanded to include τ, A_{SZ} and $\Delta^2_{\mathcal{R}}$, from which we deduce σ_8. Prior ranges and brief descriptions are given in Table 1. For further details, see *WMAP*7 and references therein. Throughout this section when stating parameter values we quote the 68.3 per cent confidence level as the associated uncertainty with all other parameters marginalized over.

3.3.1 *Covariance matrix*

In order to estimate a covariance matrix for our measured shear correlation functions in equation (8), we analyse mock CFHTLenS surveys constructed from the three-dimensional *N*-body numerical lensing simulations of Harnois-Déraps, Vafaei & Van Waerbeke (2012). The 1024^3 particle simulations have a box size of 147.0 or 231.1 h^{-1} Mpc, depending on the redshift of the simulation, and assume a flat ΛCDM cosmology parametrized by the best-fitting constraints from Komatsu et al. (2009). There are a total of 184 fully independent lines of sight spanning 12.84 deg^2 with a resolution of 0.2 arcmin sampled at 26 redshift slices in the range $0 < z < 3$. The two-point shear statistics match the theoretical predictions of the input cosmology from $0.5 < \theta < 40$ arcmin scales at all redshifts (Harnois-Déraps et al. 2012); this sets the upper angular limit for our tomographic analysis. See Heymans et al. (2012a) for a detailed discussion of covariance matrix estimation from the *N*-body simulations presented in Harnois-Déraps et al. (2012), including the required Anderson (2003) correction that we apply to de-bias our estimate of the inverse covariance matrix used in the likelihood analysis that follows.

3.3.2 *Flat ΛCDM*

We present marginalized two-dimensional likelihood constraints in the $\Omega_m - \sigma_8$ plane in Fig. 7. The best constraint from weak lensing alone is for a combination of Ω_m and σ_8, which parametrizes the degeneracy. We find $\sigma_8 \left(\frac{\Omega_m}{0.27}\right)^\alpha = 0.771 \pm 0.040$ with $\alpha = 0.553 \pm 0.016$.

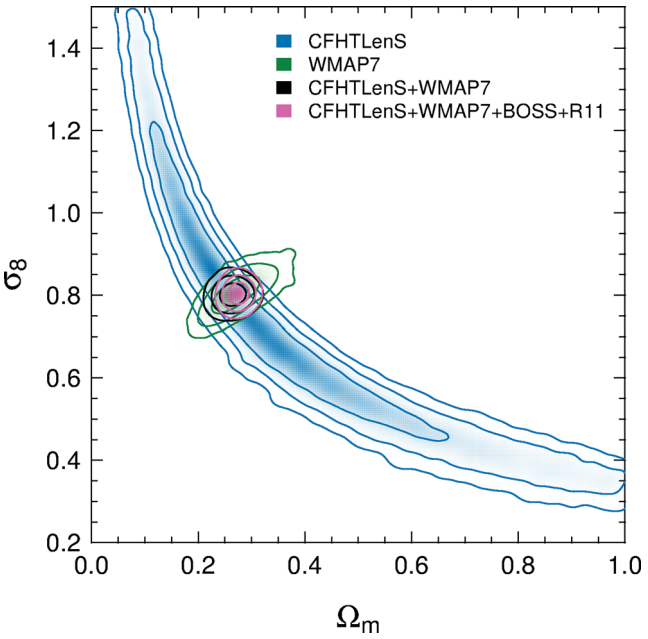

Figure 7. Marginalized parameter constraints (68.3, 95.5 and 99.7 per cent confidence levels) in the $\Omega_m - \sigma_8$ plane for a flat ΛCDM model. Results are shown for CFHTLenS (blue), *WMAP*7 (green), CFHTLenS combined with *WMAP*7 (black), and CFHTLenS combined with *WMAP*7, BOSS and R11 (pink).

When combining CFHTLenS with *WMAP*7, BOSS and R11 data sets, we find $\Omega_m = 0.2762 \pm 0.0074$ and $\sigma_8 = 0.802 \pm 0.013$. The precision is ∼20 times better than for CFHTLenS alone where we find $\Omega_m = 0.27 \pm 0.17$ and $\sigma_8 = 0.67 \pm 0.23$. Constraints on the full set of parameters are presented in Table 3. We show the results for CFHTLenS tomography, CFHTLenS combined with *WMAP*7, BOSS and R11, and, to assess the contribution of our data set to these constraints, we include results for *WMAP*7 combined with R11 and BOSS. The most valuable contribution from CFHTLenS is for Ω_m, σ_8 and Ω_b, where we improve the precision of the constraints by an average factor of 1.5.

For comparison we perform the analysis with a single redshift bin spanning the range of our two-bin analysis, $0.5 < z_p \leq 1.3$. We refer to this as the 2D lensing case, in contrast to the tomographic case where we split the galaxies into two redshift bins. Fig. 8 shows

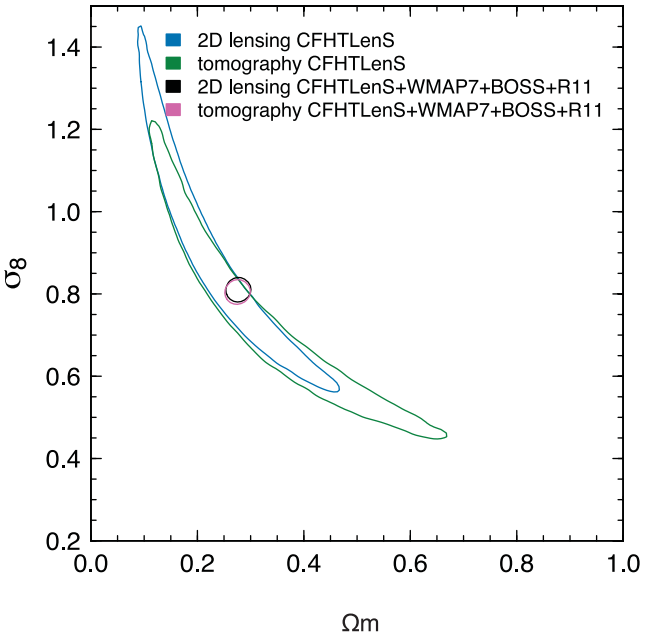

Figure 8. Marginalized parameter constraints (68.3 per cent confidence level) in the $\Omega_m - \sigma_8$ plane for a flat ΛCDM cosmology. We compare the results for 2D lensing (blue) and two-bin tomography (green). We combine CFHTLenS with *WMAP*7, BOSS and R11. Results are shown for 2D lensing (black) and two-bin tomography (pink).

Table 2. Constraints orthogonal to the $\Omega_m - \sigma_8$ degeneracy for a flat ΛCDM cosmology. Results are shown with and without highly non-linear scales which are potentially biased due to non-linear modelling and the effects of baryons (see Section 4). 'All scales' refers to scales on which the correlation functions are measured: $1 < \theta < 40$ arcmin. We remove scales corresponding to $\xi_- < 10$ arcmin in the case labelled 'Removed: $\xi_- <$ 10 arcmin'.

Data	$\sigma_8 \left(\frac{\Omega_m}{0.27}\right)^\alpha$	α
Tomography:		
All scales	0.771 ± 0.040	0.553 ± 0.016
Removed: $\xi_- < 10$ arcmin	0.776 ± 0.041	0.556 ± 0.018
2D lensing:		
All scales	0.785 ± 0.036	0.556 ± 0.018
Removed: $\xi_- < 10$ arcmin	0.780 ± 0.043	0.611 ± 0.015

the marginalized parameter constraints in the $\Omega_m - \sigma_8$ plane for both 2D lensing and tomography, and the two cases result in very similar constraints. For 2D lensing we find $\sigma_8 \left(\frac{\Omega_m}{0.27}\right)^\alpha = 0.785 \pm 0.036$ and $\alpha = 0.556 \pm 0.018$, which are in agreement with what we find for tomography (Table 2). When combining the 2D lesning results from CFHTLenS with *WMAP*7, BOSS and R11 data sets, we find $\Omega_m = 0.2774 \pm 0.0074$ and $\sigma_8 = 0.810 \pm 0.013$, which are nearly identical to those found for tomography (listed above and in Table 3). This level of agreement is also found for all other parameters when combining CFHTLenS with the other data sets. We note that all the parameter estimates agree within the 68.3 per cent errors and the sizes of the error bars from 2D lensing are very similar to those found with tomography when combining CFHTLenS with *WMAP*7, BOSS and R11 data sets.

For CFHTLenS alone, the parameter estimates for 2D lensing and tomographic lensing agree with each other within their 68.3 per cent uncertainties; however, the parameter constraints do not improve. With two broad overlapping redshift bins of average redshifts 0.7 and 1.05, there appears to be insufficient additional information to tighten parameter constraints. Previous estimates of the improvement in constraints from weak lensing tomography use non-overlapping redshift bins, Gaussian covariance and estimate errors using a Fisher matrix analysis (see Simon, King & Schneider 2004). For two redshift bins with $z < 3$ and divided at $z = 0.75$, they find the ratio of the error on individual parameters from tomography to those from a 2D analysis to be $\Delta_{tomo}/\Delta_{2D} = 0.88$. With our overlapping redshift bins and non-Gaussian covariance, it is not surprising that this marginal improvement is significantly degraded. Additionally, our 2D lensing result is for redshifts $0.5 < z_p < 1.3$; this removes low-redshift galaxies with small signal-to-noise improving constraints and weakening the gains from dividing the redshift range. We therefore expect a modest improvement at best. We find that the ratio of our tomographic errors to our 2D lensing errors is $\Delta_{tomo}/\Delta_{2D} = 1.16$. The fact that we find larger errors for tomography is surprising and warrants further discussion.

To test our covariance matrices we perform the analysis again, replacing the measured shear correlation function with that predicted from our model using a *WMAP*7 cosmology. In this case, we find that the tomographic errors are a factor of 0.98 of the 2D

Table 3. Parameter constraints with 68.3 per cent confidence limits. The following parameters are deduced for CFHTLenS: Ω_K and q_0. When combining data sets the deduced parameters are: σ_8, Ω_Λ and q_0. The label CFHTLenS+Others refers to the combination of CFHTLenS, *WMAP*7, BOSS and R11.

Parameter	Flat ΛCDM	Curved ΛCDM	Data
Ω_m	0.27 ± 0.17	0.28 ± 0.17	CFHTLenS
	0.288 ± 0.010	0.285 ± 0.014	*WMAP*7+BOSS+R11
	0.2762 ± 0.0074	0.2736 ± 0.0085	CFHTLenS+Others
σ_8	0.67 ± 0.23	0.69 ± 0.29	CFHTLenS
	0.828 ± 0.023	0.819 ± 0.036	*WMAP*7+BOSS+R11
	0.802 ± 0.013	0.795 ± 0.013	CFHTLenS+Others
Ω_Λ	$1 - \Omega_m$	0.38 ± 0.36	CFHTLenS
	$1 - \Omega_m$	0.717 ± 0.019	*WMAP*7+BOSS+R11
	$1 - \Omega_m$	0.7312 ± 0.0094	CFHTLenS+Others
Ω_K	0	0.19 ± 0.43	CFHTLenS
	0	-0.0020 ± 0.0061	*WMAP*7+BOSS+R11
	0	-0.0042 ± 0.0040	CFHTLenS+Others
h	0.84 ± 0.25	0.81 ± 0.24	CFHTLenS
	0.692 ± 0.0088	0.694 ± 0.012	*WMAP*7+BOSS+R11
	0.6971 ± 0.0081	0.693 ± 0.011	CFHTLenS+Others
Ω_b	0.030 ± 0.029	0.031 ± 0.030	CFHTLenS
	0.0471 ± 0.0012	0.0472 ± 0.0016	*WMAP*7+BOSS+R11
	$0.045\,95 \pm 0.000\,86$	0.0470 ± 0.0015	CFHTLenS+Others
q_0	-0.57 ± 0.27	-0.29 ± 0.40	CFHTLenS
	-0.568 ± 0.016	-0.574 ± 0.025	*WMAP*7+BOSS+R11
	-0.585 ± 0.011	-0.594 ± 0.014	CFHTLenS+Others
n_s	0.93 ± 0.17	0.91 ± 0.17	CFHTLenS
	0.965 ± 0.012	0.969 ± 0.014	*WMAP*7+BOSS+R11
	0.960 ± 0.011	0.972 ± 0.012	CFHTLenS+Others
τ	0.086 ± 0.014	0.086 ± 0.015	*WMAP*7+BOSS+R11
	0.081 ± 0.013	0.085 ± 0.015	CFHTLenS+Others
$\Delta^2_{\mathcal{R}}$	2.465 ± 0.086	2.45 ± 0.13	*WMAP*7+BOSS+R11
	2.429 ± 0.081	2.361 ± 0.094	CFHTLenS+Others
A_{SZ}	0.97 ± 0.62	1.35 ± 0.61	*WMAP*7+BOSS+R11
	1.33 ± 0.60	1.39 ± 0.57	CFHTLenS+Others

errors. Therefore, the increase in the tomographic errors compared to the 2D errors is not an inherent product of the covariance matrices used. This result confirms that for the case of overlapping redshift bins and non-Gaussian covariance, the expected improvement from tomography is marginal at best.

As discussed in detail in Section 4 we have also analysed the data after removing small scales which could be affected by errors in the non-linear modelling of the matter power spectrum and baryonic effects. When removing these scales ($\xi_- < 10$ arcmin) from both the tomographic and 2D lensing analyses, we see an improvement in the errors for tomography finding $\Delta_{\rm tomo}/\Delta_{\rm 2D} = 1.04$. The remaining discrepancy could be due to several factors. The Smith et al. (2003) non-linear prescription could easily be biased at the few per cent level. Residual errors in the redshift of galaxies or other per cent level systematics could be present. In addition we expect some degradation of the tomography errors due to the bias correction of the inverse covariance matrix (Anderson 2003). The covariance is estimated from a finite number of mock catalogues (see Section 3.3.1), since the tomographic covariance contains three times the number of elements as the 2D covariance, measuring it from the same number of mock catalogues results in a noisier measure. Hartlap, Simon & Schneider (2007) predict an erroneous increase in the likelihood area of 3 per cent given our number of mock catalogues 184 and the size of the data vector for 2D lensing 16 and tomography 48.

Finally, we note that our two redshift bins are chosen based on concerns of intrinsic alignment contamination; as such, they are not optimized for constraining cosmology. With more carefully selected redshift bins, it may be possible to overcome the issues discussed above and obtain improved cosmological constraints.

3.3.3 *Redshift scaling of the cosmic shear signal*

Previous CFHTLS data were found to underestimate the shear signal at high redshift, necessitating additional calibration parameters when performing cosmological fits to the data (Kilbinger et al. 2009). We demonstrate here that the CFHTLenS data have a redshift-dependent shear signal which agrees with expectations from the modelled ΛCDM cosmology.

The excellent agreement between the 2D and tomographic lensing results (Fig. 8) suggests that the shear signal across our two redshift bins scales as expected. This is also observed in the excellent agreement between the measured shear and the shear prediction based on a fiducial *WMAP*7 cosmology shown in Fig. 6.

The shear correlation function for each pair of tomographic redshift bins is analysed separately, corresponding to the shear correlation functions shown in each panel of Fig. 6. In Fig. 9 we present marginalized parameter constraints (68.3 per cent confidence level) in the $\Omega_{\rm m}$–σ_8 plane for each redshift bin combination. Since each contour is obtained from a subsample of the full data set, the degeneracy between the parameters is more pronounced and the area of the contours is larger than when analysing the full data set (Fig. 7). The agreement between the contours in Fig. 9 is a convincing demonstration that the redshift scaling of the shear in the CFHTLenS data is consistent with expectations from the modelled ΛCDM cosmology.

The power-law fits to the degenerate parameter constraints in Fig. 9 for each case are $\sigma_8 \left(\frac{\Omega_{\rm m}}{0.27}\right)^{\alpha} = 0.820 \pm 0.067$, 0.753 ± 0.053 and 0.753 ± 0.050 with $\alpha = 0.662 \pm 0.020, 0.621 \pm 0.016$ and 0.535 ± 0.013 for the low–low, low–high and high–high redshift bin pairings, respectively. Note the expected evolution of α with redshift.

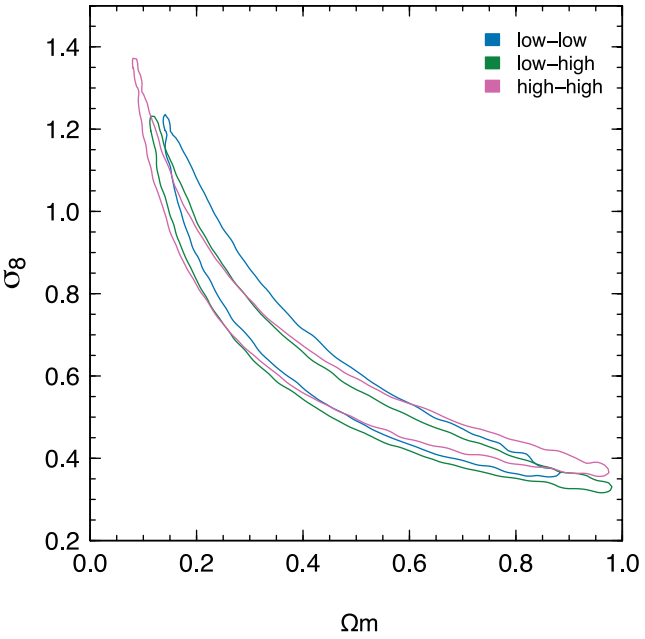

Figure 9. Marginalized parameter constraints (68.3 per cent confidence level) in the $\Omega_{\rm m}$–σ_8 plane for a flat ΛCDM cosmology. The results are shown for each combination of the two redshift bins. The low- and high-redshift bins correspond to $0.5 < z_{\rm p} \leq 0.85$ and $0.85 < z_{\rm p} \leq 1.3$, respectively. The excellent agreement shows that redshift scaling of the signal is consistent with the modelled ΛCDM cosmology.

We reiterate that the cosmological model-dependent verification of redshift scaling presented here is completely independent of the calibration of the data and the rejection of bad fields, which were done with tests which are not sensitive to cosmology (Heymans et al. 2012b).

3.3.4 *Curved ΛCDM*

A curved ΛCDM cosmology is modelled, for the full details of parameters and priors used see Table 1. We present constraints in the $\Omega_{\rm m}$–σ_8 and $\Omega_{\rm m}$–Ω_Λ planes in Fig. 10. One-dimensional marginalized results when combining CFHTLenS with *WMAP*7, BOSS and R11 are $\Omega_{\rm m} = 0.2736 \pm 0.0085$, $\Omega_\Lambda = 0.7312 \pm 0.0094$, $\Omega_{\rm K} = -0.0042 \pm 0.0040$ and $\sigma_8 = 0.795 \pm 0.013$. The constraints on $\Omega_{\rm m}$ and σ_8 do not change significantly from the flat ΛCDM case. Parameter constraints for both models are presented in Table 3. The addition of CFHTLenS to *WMAP*7, BOSS and R11 is most helpful at constraining $\Omega_{\rm m}$, σ_8, $\Omega_{\rm K}$ and Ω_Λ. The precision for these parameters improves, on average, by a factor of 2.

We again find excellent agreement with the 2D lensing analysis. When combining the 2D lensing of CFHTLenS with *WMAP*7, BOSS and R11 data sets, we find $\Omega_{\rm m} = 0.2766 \pm 0.0082$, $\Omega_\Lambda = 0.7273 \pm 0.0089$, $\Omega_{\rm K} = -0.0035 \pm 0.0035$ and $\sigma_8 = 0.804 \pm 0.016$. We do not show the complete details of our 2D lensing parameter estimations. However, we note that in all cases, either with CFHTLenS alone or combined with the other cosmological probes, the 2D results agree with the tomographic results within the 68.3 per cent errors and the size of the error bars is similar for both cases. We again find that for CFHTLenS alone, the ratio of individual parameter uncertainties from the tomographic analysis to those of the 2D lensing analysis is $\Delta_{\rm tomo}/\Delta_{\rm 2D} = 1.16$.

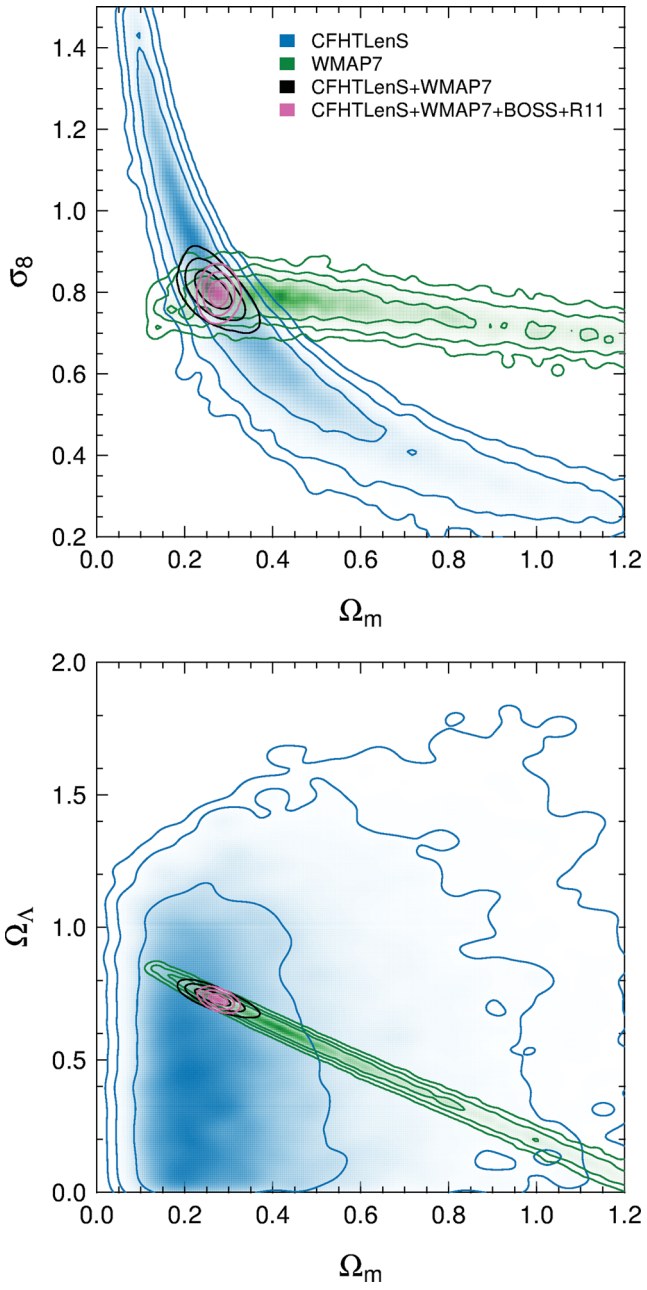

Figure 10. Marginalized parameter constraints (68.3, 95.5 and 99.7 per cent confidence levels) for a curved ΛCDM cosmology. Results are shown for CFHTLenS (blue), *WMAP*7 (green), CFHTLenS combined with *WMAP*7 (black), and CFHTLenS combined with *WMAP*7, BOSS and R11 (pink). Top panel: constraints in the $\Omega_m - \sigma_8$ parameter space. Bottom panel: constraints in the $\Omega_m - \Omega_\Lambda$ parameter space.

3.3.5 *Constraining the deceleration parameter*

The deceleration parameter q_0 parametrizes the change in the expansion rate of the Universe. We calculate this as a deduced parameter for both the flat and the curved ΛCDM models. The deceleration parameter depends on the energy density parameters

$$q_0 \equiv -\frac{\ddot{a}(t_0)a(t_0)}{\dot{a}^2(t_0)} = \frac{\Omega_m}{2} - \Omega_\Lambda \quad \text{(curved } \Lambda\text{CDM)}$$

$$= \frac{3\Omega_m}{2} - 1 \quad \text{(flat } \Lambda\text{CDM)}, \tag{14}$$

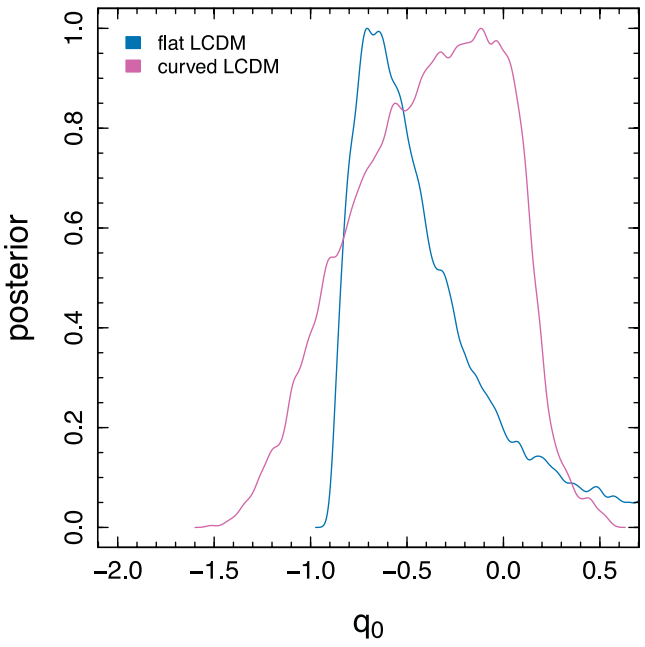

Figure 11. Marginalized constraints on the deceleration parameter using the CFHTLenS two-bin tomographic weak lensing results. An accelerating universe ($q_0 < 0$) is found at the 82 per cent confidence level for a curved ΛCDM model (pink), and at the 89 per cent confidence level for a flat ΛCDM model (blue).

where the scale factor at present time is $a(t_0)$ and derivatives with respect to time are denoted with a dot. For the flat case, q_0 is simply a transformation of our results for the matter density parameter Ω_m. We present marginalized constraints for q_0 in Fig. 11. The pink line is for the curved case where we find $q_0 = -0.29 \pm 0.40$, and the blue line is for the flat case where we find $q_0 = -0.57 \pm 0.27$. Negative values indicate acceleration of the expansion of the Universe. Summing the posterior for $q_0 < 0$ gives us the confidence level at which we have measured an accelerating Universe. For the curved and flat models, we find that $q_0 < 0$ at the 82 and 89 per cent confidence level, respectively.

Schrabback et al. (2010) constrain q_0 with a six-bin tomographic analysis of the COSMOS-30 data. Besides having more tomographic bins, the redshift range probed is also greater, extending to $z = 4$. For a curved ΛCDM cosmology, holding Ω_b and n_s fixed and using a Gaussian prior on the Hubble constant of $h = 0.72 \pm 0.025$, they find $q_0 < 0$ at 96 per cent confidence. If we do a similar analysis with Ω_b and n_s held fixed and using the a Gaussian prior of $h = 0.738 \pm 0.024$ (R11), we find $q_0 < 0$ at 84 per cent confidence. The difference in constraints on the deceleration parameter can be understood as a result of the much larger values of the dark energy density preferred by COSMOS-30 $\Omega_\Lambda = 0.97^{+0.39}_{-0.60}$, which lead to smaller values of q_0, whereas the dark energy density found here from CFHTLenS is $\Omega_\Lambda = 0.38 \pm 0.36$, resulting in larger values of q_0 for CFHTLenS.

With CFHTLenS alone, we are not able to put a strong constraint on the acceleration of the expansion of the Universe. With the addition of the other cosmological probes, the entire posterior distribution of q_0 is less than zero. For a curved model with CFHTLenS combined with the other probes, we find $q_0 = -0.594 \pm 0.014$ (see Table 3). An accelerating Universe is unambiguously detected.

4 IMPACT OF NON-LINEAR EFFECTS AND BARYONS ON THE TOMOGRAPHIC COSMOLOGICAL CONSTRAINTS

We have presented cosmological parameter constraints from an analysis of the tomographic two-point shear correlation function $\xi_{\pm}^{k,l}(\theta)$ (equation 11), incorporating the non-linear dark matter only power spectrum from Smith et al. (2003) as our theoretical model of $P_\delta(k, z)$ in equation (12). Note that $k = \ell(f_K(\chi))^{-1}$. This halo-model prescription for the non-linear correction has been calibrated on numerical simulations and shown to have an accuracy of 5−10 per cent over a wide range of scales (Eifler 2011). The *N*-body simulations used to estimate the covariance matrices used in this analysis suggest that the accuracy is even better than this for a *WMAP*5 cosmology (Harnois-Déraps et al. 2012) over the redshift range covered in this analysis. While these comparisons give us confidence in our results, and suggest that any error from the non-linear correction will be small in comparison to our statistical error, it is prudent to assess how errors in the non-linear correction will impact our results.

A fully 3D weak lensing analysis of the CFHTLenS data is presented in Kitching et al. (in preparation). This power spectrum analysis allows for exact redshift-dependent cuts in the wavevector k, which can be motivated by either the comparison of the power spectrum measured from *N*-body simulations to the non-linear prescription or the selection of linear scales where the non-linear correction is negligible. For real-space statistics, as used in this paper and in Kilbinger et al. (2013), it is not possible to make an unambiguous separation of scales. The two-point correlation function $\xi_{\pm}^{k,l}(\theta)$ is related to the underlying matter power spectrum $P_\delta(k, z)$ through integrals over k and z, modulated by the lensing efficiency $g(z)$ (equation 13) and Bessel functions $J_{0/4}(\ell\theta)$ for $\xi_{+/-}(\theta)$ (see equations 11 and 12). The measured tomographic two-point shear correlation function $\xi_{\pm}^{k,l}$ at a fixed scale θ therefore probes a range of k in the underlying matter power spectrum. In addition, owing to the different Bessel functions, ξ_+ preferentially probes much smaller k, and hence larger physical scales, than ξ_-.

Kilbinger et al. (2013) present an analysis of the 2D shear correlation function out to large angular scales $\theta < 350$ arcmin. The consistent constraints obtained from the large quasi-linear regime $\theta > 53$ arcmin in comparison to the full angular range, analysed using the Smith et al. (2003) non-linear power spectrum, give us confidence that the accuracy of this correction is sufficient, falling within our statistical errors.

Comparing the theoretical expectation of $\xi_{\pm}^{k,l}(\theta)$ (equation 11) for a *WMAP*7 cosmology, calculated using a non-linear and a linear power spectrum, we determine the angular scale below which the non-linear and linear models differ in amplitude by greater than 10 per cent. For ξ_+, this quasi-linear limit ranges from 10 to 14 arcmin for the three different tomographic combinations (the lowest redshift bin requiring the largest θ cut). For ξ_-, the quasi-linear limit ranges from 100 to 140 arcmin. In this analysis, we limit our angular range to scales with $\theta \lesssim 40$ arcmin where we can accurately assess a covariance matrix from the lensing simulations (Harnois-Déraps et al. 2012). We are therefore unable to follow Kilbinger et al. (2013) by limiting our real-space analysis to this quasi-linear regime as we do not probe sufficiently large angular scales. We can however make an assessment of how an error on the non-linear correction would impact our results. We first compare the *WMAP*7 theoretical expectation of $\xi_{\pm}^{k,l}(\theta)$ calculated using a non-linear correction boosted by 7 per cent, with a model calculated with the non-linear correction decreased by 7 per cent. Note that we choose the value of 7 per cent from the average error over the range of k tested in Eifler (2011). We find that these two limits on the non-linear correction cause at least a 10 per cent change in the amplitude of $\xi_{\pm}^{k,l}(\theta)$ for scales $\theta \lesssim 1$ arcmin for ξ_+ and $\theta \lesssim 10$ arcmin for ξ_-. Applying these cuts in angular scale corresponds to removing the first five angular scales for ξ_- for each tomographic bin shown in Fig. 6. All ξ_+ scales remain in the analysis. With these scales removed, any remaining uncertainty due to the non-linear modelling is well within our statistical error.

For reference, we calculate the approximate wavenumber corresponding to the physical separation of the source galaxies when the small-scale cuts are applied. Using the relation $k = 2\pi(\theta f_K(\chi))^{-1}$, and assuming a flat ΛCDM cosmology, the angular scale cuts correspond to wavenumbers $k_{\theta=1'} \sim 12\,h\,\mathrm{Mpc}^{-1}$ and $k_{\theta=10'} \sim 1.2\,h\,\mathrm{Mpc}^{-1}$. Here we have calculated the angular diameter distance to the mean redshift of the low-redshift bin $f_K(\chi) = 1800\,h^{-1}\,\mathrm{Mpc}$. To determine what wavenumber the shear correlation functions are sensitive to, we must account for the Bessel functions, power spectrum and lensing efficiency in equations (11) and (12). To get a rough estimate we take the power spectrum to be a pure power law with exponent −2, and take the mid-point of the angular diameter distance since this is approximately where the lensing efficiency will peak $f_K(\chi) \sim 900\,h^{-1}\,\mathrm{Mpc}$. We perform the integral in equation (11) for both ξ_+ and ξ_- and note for which ℓ 90 per cent of the final value is reached. This results in an approximate wavenumber of $k \sim 2.5\,h\,\mathrm{Mpc}^{-1}$ for both ξ_+ and ξ_-.

Fig. 12 compares cosmological parameter constraints in the $\Omega_\mathrm{m}-\sigma_8$ plane for this limited number of scales in comparison to the full data set analysed in Section 3. The removal of small scales results in a slight change to the degeneracy of the parameters. This

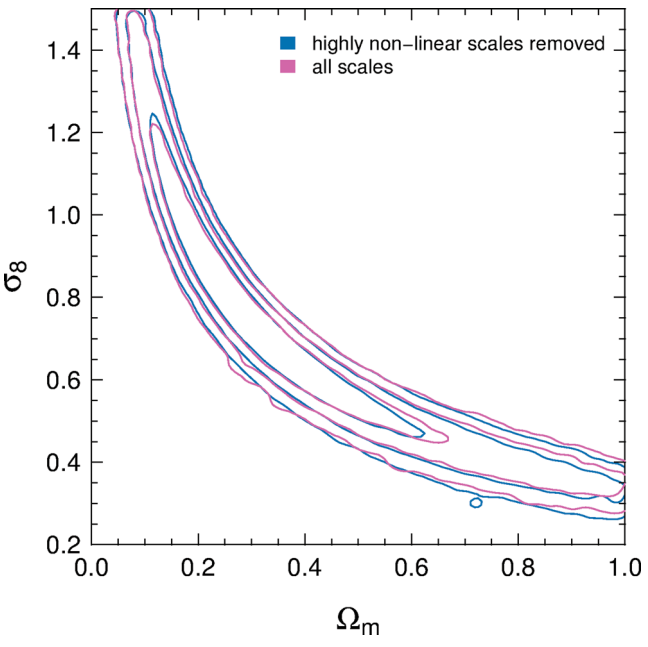

Figure 12. Marginalized parameter constraints (68.3, 95.5 and 99.7 per cent confidence levels) in the $\Omega_\mathrm{m}-\sigma_8$ plane for a flat ΛCDM cosmology. The pink contours show the result when all eight scales are included; this is the same as the result for CFHTLenS shown in Fig. 7. The blue contours show the result of removing highly non-linear scales, which are possibly biased due to the non-linear correction to the matter power spectrum or the effect of baryons. We remove the five smallest scales of ξ_-, corresponding to $\theta <$ 10 arcmin. The contours are only slightly different, indicating that we are not sensitive to these effects given the level of precision of our results.

test gives us confidence that the non-linear correction used is sufficiently accurate given the statistical error of the survey. This is unlikely to be true for future surveys, where the increased statistical accuracy will require better knowledge of the non-linear correction to the power spectrum (Eifler 2011).

Finally we turn to the impact of baryons on our results. In our analysis, we assume that the underlying matter power spectrum is sufficiently well represented by the non-linear dark matter only power spectrum, neglecting the role of baryons. The impact of baryons on the power spectrum is sensitive to the baryonic feedback model used. Therefore, the magnitude of the impact of baryons remains uncertain. Semboloni et al. (2011) present an analysis of cosmological hydrodynamic simulations to quantify the effect of baryon physics on the weak gravitational lensing shear signal using a range of different baryonic feedback models. Their work suggests that a conservative weak lensing analysis should be limited to those scales where $k \lesssim 1.5\,h\,\mathrm{Mpc}^{-1}$. We implement such a conservative scheme in the 3D power spectrum analysis of Kitching et al. (in preparation). As discussed above, our real-space analysis mixes k and z scales, leaving us unable to perform a similarly clear test here.

Semboloni et al. (2011) also present a comparison of $\xi_{\pm}^{k,l}(\theta)$ measured for both the cosmological hydrodynamic simulations and a dark matter only simulation for different redshifts, which we use to judge the level of error we should expect baryons to introduce. Assuming the realistic AGN feedback model, and considering the scales used in the conservative analysis of Fig. 12 ($\theta \geq 1.34$ arcmin and $\theta \geq 15.4$ arcmin for ξ_+ and ξ_-, respectively), we expect baryons to cause a decrease in the modelled signal of less than 10 per cent. The fact that we see very little difference between the conservative and full analysis presented in Fig. 12 demonstrates that the underlying matter power spectrum is indeed sufficiently well represented by the non-linear dark matter only power spectrum for our statistical accuracy. It also indicates that the impact of baryons on the non-linear dark matter only power spectrum is unlikely to be larger than that predicted by Semboloni et al. (2011). However, baryonic effects will have to be carefully considered for the next generation of weak lensing surveys that will have significantly smaller statistical errors. Semboloni, Hoekstra & Schaye (2012) show the importance of baryonic effects on three-point shear statistics and propose a modification to the modelling of the non-linear matter power spectrum to account for these effects.

5 CONCLUSION

The most important result of this study is that the sum of the photometric redshift PDFs within a redshift bin provides an accurate measure of the true redshift distribution of those galaxies, accounting for the scatter due to catastrophic as well as statistical errors. To demonstrate the accuracy of the PDFs, we have compared the summed PDFs with the redshift distribution predicted by spectroscopic redshifts, resampled COSMOS-30 redshifts and predictions from a redshift contamination analysis using the angular correlation function. We find excellent agreement for the redshift range $z_\mathrm{p} < 1.3$. This result indicates that the priors and spectral templates used in Hildebrandt et al. (2012) to derive the photometric redshifts provide an accurate and complete description of the galaxies at $z_\mathrm{p} < 1.3$. This also motivates our use of the summed PDF as a measure of the redshift distributions in our tomographic weak lensing analysis. Furthermore, the proven accuracy of the summed PDFs provides a reliable method for estimating the source redshift distribution in future weak lensing studies.

We have performed a cosmological analysis of the CFHTLenS data on angular scales $1 < \theta < 40$ arcmin, using two broad redshift bins, $0.5 < z_\mathrm{p} \leq 0.85$ and $0.85 < z_\mathrm{p} \leq 1.3$, which are not significantly affected by the intrinsic alignment of galaxy shapes. We model two cosmologies: flat and curved ΛCDM. Due to complementary degeneracies, our results add valuable constraining power when combined with those from the CMB (*WMAP*7), BAOs (BOSS) and a prior on the Hubble constant (R11). The addition of our weak lensing results to these other cosmological probes increases the precision of individual marginalized parameter constraints by an average factor of 1.5−2.

For a flat ΛCDM model, the joint parameter constraints for CFHTLenS, *WMAP*7, BOSS and R11 are $\Omega_\mathrm{m} = 0.2762 \pm 0.0074$ and $\sigma_8 = 0.802 \pm 0.013$. For a curved ΛCDM model, combining the same data sets, we find $\Omega_\mathrm{m} = 0.2736 \pm 0.0085$, $\Omega_\Lambda = 0.7312 \pm 0.0094$, $\Omega_\mathrm{K} = -0.0042 \pm 0.0040$ and $\sigma_8 = 0.795 \pm 0.013$. Full details of our parameter estimates for both cosmologies are presented in Table 3. Our results are consistent with those presented in other studies of the CFHTLenS data: a 2D lensing analysis probing much larger scales where linear theory provides a more accurate model to the matter power spectrum (Kilbinger et al. 2013) and a fine-binned tomographic analysis with six redshift bins accounting for intrinsic alignments (Heymans et al. 2012a).

We compare the tomographic constraints with those from a 2D lensing analysis spanning the same range of redshift $0.5 < z_\mathrm{p} \leq 1.3$. We find the two analyses to be completely consistent with all parameter estimates agreeing within their 68.3 per cent confidence levels. We note that the ratio of uncertainties on individual parameters from tomography to those from 2D lensing is on average $\Delta_\mathrm{tomo}/\Delta_\mathrm{2D} = 1.16$. This statistic is 0.98 if we replace our data vectors with a fiducial model, indicating that our covariance matrices do show a slight improvement for tomography. We argue that our non-Gaussian covariance and broad overlapping redshift bins degrade the modest improvement ($\Delta_\mathrm{tomo}/\Delta_\mathrm{2D} = 0.88$) expected from idealized Fisher matrix calculations (Simon et al. 2004). We identify small scales as being largely responsible for the observed increase, finding $\Delta_\mathrm{tomo}/\Delta_\mathrm{2D} = 1.04$ when these scales are removed from the analyses. These scales could be biased due to uncertainties in the modelling of the non-linearities in the matter power spectrum and baryonic effects. Although small scales have inflated our uncertainties from tomography, we show in Section 4 that they do not significantly affect our results.

Previous analyses of CFHTLS data were hindered by a strong redshift-dependent bias in the weak lensing shear, necessitating additional nuisance parameters when analysing the tomographic shear (Kilbinger et al. 2009). We demonstrate that the redshift scaling of the CFHTLenS cosmic shear signal agrees with expectations from the modelled ΛCDM cosmology. The strongest test of this is presented in Fig. 9, which shows the agreement of cosmological constraints measured for each combination of redshift bins in the $\Omega_\mathrm{m}-\sigma_8$ plane for a flat ΛCDM cosmology. This demonstrates the effectiveness of the cosmology-independent tests of residual systematics presented in Heymans et al. (2012b), including the rejection of 25 per cent of the MegaCam pointings which failed to pass these tests. Note also that the shear calibration performed on numerical simulations (Miller et al. 2013) was completed before any cosmological analysis was performed on the data. The two-bin analysis presented here is sensitive to redshift-dependent cosmology without introducing additional parameters to model intrinsic

alignments, as such it is an excellent final test of the CFHTLenS data product.

ACKNOWLEDGEMENTS

This work is based on observations obtained with MegaPrime/MegaCam, a joint project of CFHT and CEA/DAPNIA, at the Canada–France–Hawaii Telescope (CFHT) which is operated by the National Research Council (NRC) of Canada, the Institut National des Sciences de l'Univers of the Centre National de la Recherche Scientifique (CNRS) of France and the University of Hawaii. This research used the facilities of the Canadian Astronomy Data Centre operated by the National Research Council of Canada with the support of the Canadian Space Agency. We thank the CFHT staff for successfully conducting the CFHTLS observations and in particular Jean-Charles Cuillandre and Eugene Magnier for the continuous improvement of the instrument calibration and the Elixir detrended data that we used. We also thank TERAPIX for the quality assessment and validation of individual exposures during the CFHTLS data acquisition period, and Emmanuel Bertin for developing some of the software used in this study. CFHTLenS data processing was made possible thanks to significant computing support from the NSERC Research Tools and Instruments grant programme, and to HPC specialist Ovidiu Toader. The early stages of the CFHTLenS project were made possible thanks to the support of the European Commissions Marie Curie Research Training Network DUEL (MRTN-CT-2006-036133) which directly supported LF, HHi, BR and MV between 2007 and 2011 in addition to providing travel support and expenses for team meetings.

The *N*-body simulations used in this analysis were performed on the TCS supercomputer at the SciNet HPC Consortium. SciNet is funded by the Canada Foundation for Innovation under the auspices of Compute Canada, the Government of Ontario, Ontario Research Fund – Research Excellence and the University of Toronto.

LVW acknowledges support from the Natural Sciences and Engineering Research Council of Canada. CH and FS acknowledge support from the European Research Council under the EC FP7 grant number 240185. TE is supported by the Deutsche Forschungsgemeinschaft through project ER 327/3-1 and the Transregional Collaborative Research Centre TR 33 – 'The Dark Universe'. HHo and ES acknowledge support from Marie Curie IRG grant 230924, the Netherlands Organization for Scientific Research (NWO) grant number 639.042.814 and from the European Research Council under the EC FP7 grant number 279396. HHi is supported by the Marie Curie IOF 252760, a CITA National Fellowship and the DFG grant Hi 1495/2-1. TDK acknowledges support from a Royal Society University Research Fellowship (NSERC) and the Canadian Institute for Advanced Research (CIfAR, Cosmology and Gravity programme). YM acknowledges support from CNRS/INSU (Institut National des Sciences de l'Univers) and the Programme National Galaxies et Cosmologie (PNCG). BR acknowledges support from the European Research Council in the form of a Starting Grant with number 24067. TS acknowledges support from NSF through grant AST-0444059-001, SAO through grant GO0-11147A and NWO. LF acknowledges support from NSFC grants 11103012 and 10878003, Innovation Programme 12ZZ134 and Chen Guang project 10CG46 of SMEC, and STCSM grant 11290706600 and Pujiang Programme 12PJ1406700. MJH acknowledges support from the Natural Sciences and Engineering Research Council of Canada (NSERC). MV acknowledges support from the Netherlands Organization for Scientific Research (NWO) and from the Beecroft Institute for Particle Astrophysics and Cosmology.

Author Contributions. All authors contributed to the development and writing of this paper. The authorship list reflects the lead authors of this paper (JB, LVW, CH and MK) followed by two alphabetical groups. The first alphabetical group includes key contributors to the science analysis and interpretation in this paper, the founding core team and those whose long-term significant effort produced the final CFHTLenS data product. The second group covers members of the CFHTLenS team who made a significant contribution to either the project, this paper, or both. The CFHTLenS collaboration was co-led by CH and LVW and the CFHTLenS Cosmology Working Group was led by TK.

REFERENCES

Albrecht A. et al., 2006, preprint (astro-ph/0609591)
Albrecht A. et al., 2009, preprint (arXiv:0901.0721)
Anderson T. W., 2003, An Introduction to Multivariate Statistical Analysis. Wiley, New York
Anderson L. et al., 2012, MNRAS, 427, 3435 (BOSS)
Bacon D. J., Massey R. J., Refregier A. R., Ellis R. S., 2003, MNRAS, 344, 673
Bacon D. J. et al., 2005, MNRAS, 363, 723
Bartelmann M., Schneider P., 2001, Phys. Rep., 340, 291
Benítez N., 2000, ApJ, 536, 571
Benjamin J. et al., 2007, MNRAS, 381, 702
Benjamin J., Van Waerbeke L., Ménard B., Kilbinger M., 2010, MNRAS, 408, 1168
Bernstein G., Huterer D., 2010, MNRAS, 401, 1399
Bridle S., King L., 2007, New J. Phys., 9, 444
Brodwin M., Lilly S. J., Porciani C., McCracken H. J., Le Fèvre O., Foucaud S., Crampton D., Mellier Y., 2006, ApJS, 162, 20
Brown M. L., Taylor A. N., Hambly N. C., Dye S., 2002, MNRAS, 333, 501
Capak P. et al., 2004, AJ, 127, 180
Cappé O., Douc R., Guillin A., Marin J. M., Robert C. P., 2007, preprint (arXiv:0710.4242)
Croft R. A. C., Metzler C. A., 2000, ApJ, 545, 561
Cunha C. E., Lima M., Oyaizu H., Frieman J., Lin H., 2009, MNRAS, 396, 2379
Eifler T., 2011, MNRAS, 418, 536
Eisenstein D. J., Hu W., 1998, ApJ, 496, 605
Erben T. et al., 2012, preprint (arXiv:1210.8156)
Feldmann R. et al., 2006, MNRAS, 372, 565
Fu L. et al., 2008, A&A, 479, 9
Hamana T. et al., 2003, ApJ, 597, 98
Harnois-Déraps J., Vafaei S., Van Waerbeke L., 2012, MNRAS, 426, 1262
Hartlap J., Simon P., Schneider P., 2007, A&A, 464, 399
Hearin A. P., Zentner A. R., Ma Z., Huterer D., 2010, ApJ, 720, 1351
Heavens A., Refregier A., Heymans C., 2000, MNRAS, 319, 649
Heymans C. et al., 2012a, MNRAS, submitted
Heymans C. et al., 2012b, MNRAS, 427, 146
Hildebrandt H., Pielorz J., Erben T., Van Waerbeke L., Simon P., Capak P., 2009, A&A, 498, 725
Hildebrandt H. et al., 2012, MNRAS, 421, 2355
Hirata C. M., Seljak U., 2004, Phys. Rev. D, 70, 063526
Hoekstra H. et al., 2006, ApJ, 647, 116
Hu W., 1999, ApJ, 522, L21
Huterer D., 2002, Phys. Rev. D, 65, 063001
Ilbert O. et al., 2009, ApJ, 690, 1236
Jarvis M., Bernstein G. M., Fischer P., Smith D., Jain B., Tyson J. A., Wittman D., 2003, AJ, 125, 1014
Kilbinger M. et al., 2009, A&A, 497, 677
Kilbinger M. et al., 2010, MNRAS, 405, 2381
Kilbinger M. et al., 2011, preprint (arXiv:1101.0950)
Kilbinger M. et al., 2013, MNRAS, in press

Komatsu E. et al., 2009, ApJS, 180, 330
Komatsu E. et al., 2011, ApJS, 192, 18 (*WMAP*7)
Landy S. D., Szalay A. S., 1993, ApJ, 412, 64
Le Fèvre O. et al., 2005, A&A, 439, 845
Lima M., Cunha C. E., Oyaizu H., Frieman J., Lin H., Sheldon E. S., 2008, MNRAS, 390, 118
Ma Z., Hu W., Huterer D., 2006, ApJ, 636, 21
Mandelbaum R. et al., 2008, MNRAS, 386, 781
Massey R. et al., 2007, ApJS, 172, 239
Miller L. et al., 2013, MNRAS, 429, 2858
Newman J. A. et al., 2012, preprint (arXiv:1203.3192)
Peacock J. A., Schneider P., Efstathiou G., Ellis J. R., Leibundgut B., Lilly S. J., Mellier Y., 2006, Technical Report, ESA–ESO Working Group on 'Fundamental Cosmology'
Riess A. G. et al., 2011, ApJ, 730, 119 (R11)
Schrabback T. et al., 2010, A&A, 516, A63
Semboloni E. et al., 2006, A&A, 452, 51
Semboloni E., Hoekstra H., Schaye J., van Daalen M. P., McCarthy I. G., 2011, MNRAS, 417, 2020
Semboloni E., Hoekstra H., Schaye J., 2012, preprint (arXiv:1210.7303)
Simon P., King L. J., Schneider P., 2004, A&A, 417, 873
Simpson F. et al., 2013, MNRAS, 429, 2249
Smith R. E. et al., 2003, MNRAS, 341, 1311
Van Waerbeke L., Mellier Y., Pelló R., Pen U. L., McCracken H. J., Jain B., 2002, A&A, 393, 369
Van Waerbeke L., Mellier Y., Hoekstra H., 2005, A&A, 429, 75
Van Waerbeke L., White M., Hoekstra H., Heymans C., 2006, Astropart. Phys., 26, 91
Wall J. V., Jenkins C. R., 2003, in Ellis R., Huchra J., Kahn S., Rieke G., Stetson P. B., eds, Practical Statistics for Astronomers. Cambridge Univ. Press, Cambridge, p. 96
Wittman D., 2009, ApJ, 700, L174
Wraith D., Kilbinger M., Benabed K., Cappé O., Cardoso J. F., Fort G., Prunet S., Robert C. P., 2009, Phys. Rev. D, 80, 023507

This paper has been typeset from a TEX/LATEX file prepared by the author.